Novel Phenomena in Modern Studies of Magnetism

by

Imam Makhfudz

A dissertation submitted to The Johns Hopkins University in conformity with the requirements for the degree of Doctor of Philosophy.

Baltimore, Maryland

December, 2013

Abstract

In this PhD Dissertation, we present investigation of contemporary problems in magnetism. We focus on two important themes that have been active research topics in condensed matter community: 1. Topological defects in magnet and their dynamics 2. Exotic states and critical phenomena in frustrated spin systems.

In the first topic, we consider the dynamics of topological defect known as Skyrmion in thin film ferromagnet. We first discuss the nontrivial dynamics exhibited by a Skyrmion bubble confined in thin film disk as observed by numerical simulation. We propose a phenomenological theory that can reproduce the peculiar dynamics of the Skyrmion bubble. We show that, unlike previously studied topological defects, a Skyrmion bubble possesses inertia. We derive a theoretical description of the dynamics using standard theory of ferromagnet. We discover the presence of two counter propagating chiral edge modes. Most importantly, we derive the mass (inertia) from the theory and express it in terms of microscopic parameters.

In the second topic, a quantum phase transition in $U(1)$ quantum spin liquid phase of 3-d pyrochlore quantum spin ice is investigated. Starting from microscopic

ABSTRACT

spin model, we map the spin to slave-boson, derive continuum theory, and finally arrive at a $U(1)$ gauge theory which takes the form of scalar quantum electrodynamics (QED). The effective free energy for quantum spin liquid (QSL) to antiferromagnetic (AFM) phase transition mimics the one for Bardeen-Cooper-Schrieffer (BCS) superconductors classical transition under magnetic field. We show that, provided Ginzburg criterion is satisfied, the gauge field fluctuations drive the originally continuous QSL to AFM phase transition at mean field level into discontinuous one. We predict the location of quantum critical point which agrees well with gauge mean field theory result. We calculate the size of phase transition and find that it is a weakly first order.

Primary Reader: Oleg Tchernyshyov

Secondary Reader: Predrag Nikolic

Committee: Oleg Tchernyshyov, Collin Broholm, Jared Kaplan, Michael Falk, Jacob Khurgin

Acknowledgments

I would like thank Prof. Oleg Tchernyshyov for the guidance and supervision during my PhD years at Johns Hopkins University.

Dedication

This thesis is dedicated to my father Hartono and my mother Eni Ansorwati.

Contents

List of Figures

Chapter 1

Introduction

1.1 Dynamics of a Skyrmion Bubble

1.1.1 Topological Defects in Thin Film Ferromagnet

Topological defects refer to configurations of field or order parameter that are topologically distinct from vacuum in the sense that they cannot be smoothly connected to vacuum and are characterized by nontrivial value of topological invariant and properties that are stable against perturbations. In the context of magnetism, topological defects refer to configurations of magnetization vector field (in classical magnetism) or of spins (in quantum magnetism) that are topologically distinct from vacuum in the form of smooth configuration of magnetization or spins such as ferro-

magnetically ordered state.

Ferromagnetic order is characterized by magnetization vector field uniformly polarized in parallel direction along certain orientation. Deformation away from this uniform magnetization represents defect. Small deformations of magnetization vector field in ferromagnet lead to spin wave in configurations that are still smoothly connected to parallel magnetization configuration of ferromagnet. There can however be deformations, i.e. defects, which are not smooth and cannot be smoothly connected to uniform magnetization of ferromagnetic state. These deformations (defects) turn out to be also topological in character; i.e. they acquire nontrivial topological structure. These are topological defects in magnet.

Topological defects are interesting both from pure scientific interest and potential practical applications. One of the most active subjects of research with regard to topological defects is their dynamics. Topological defects in magnet have been found to display nontrivial dynamics when subject to external driving force such as applied magnetic field. This nontrivial dynamics is precisely the source of potential applications of topological defects in magnet, ranging from memory device to high speed computing.

Topological defects normally involve variation of magnetization configuration. Oldest studies of topological defects in magnet started with the simplest of those structures; the domain wall. Straight domain wall and its dynamics was first studied by Walker [1] and others. We will focus on topological defect called Skyrmion.

1.1.2 Skyrmion and Topology

Topological defects in magnet have long been studied and classified based on the topological properties satisfied by the configuration of magnetization that makes up the defects [2]. In general, topology ensures the stability of the magnetization texture against weak perturbation once the structure is formed. We will not focus much on the topology of defects in magnet but it is useful to describe some topological aspects of the Skyrmion which is studied in this Thesis.

The concept of Skyrmion first arose in the field of nuclear physics following the work of Tony Skyrme who tried to explain the structure of nucleon [3]. Magnetization points down at the center of the skyrmion and up at infinity, interpolating through in-plane directions in between, Fig. 1.1.

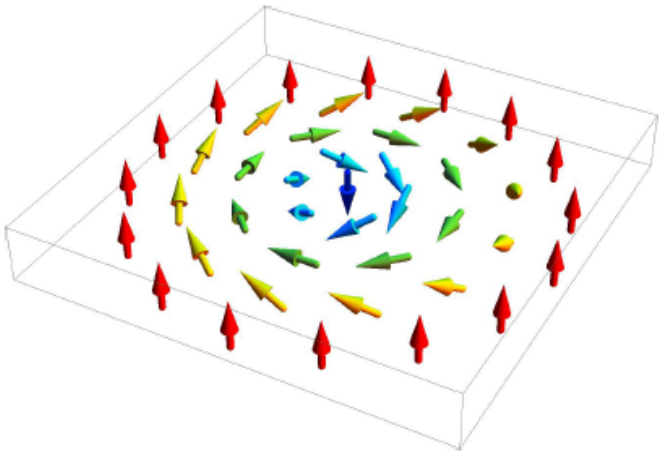

Figure 1.1: The profile of a Skyrmion

In the language of topology and manifold, magnetization pattern on 2-d plane is a mapping from $\mathbb{R}^2 \to \mathbb{R}^3$. At temperatures well below Curie's temperature however,

the magnetization magnitude is fixed and therefore we have $\mathbb{R}^2 \to \mathbb{R}^2$ mapping. Other than this mathematical consideration, from physical consideration we know that for any magnetization configuration to have (bounded) finite energy, the magnetization vector must take a fixed constant value at infinite distances. This is also the case with the Skyrmion structure above where either $\mathbf{m} = m\hat{\mathbf{z}}$ or $\mathbf{m} = -m\hat{\mathbf{z}}$ at $r \to \infty$. Mathematically speaking, such vector configurations originally living in $\mathbb{R}^2$ can be mapped to $\mathbb{S}^2$, which is a sphere in three dimensions, where the fixed magnetization vector at infinity is stereographically projected to a point on the sphere, e.g. the north pole. If we consider an infinite 2-d (e.g. $x\,y$) plane, it can also be mapped to a $\mathbb{S}^2$ sphere with points at infinite distance on the plane be mapped to the north pole of the sphere, for example. In the end therefore, our magnetization structure including this Skyrmion we are studying, can be classified as a mapping $\mathbb{S}^2 \to \mathbb{S}^2$; this is called second homotopy group in topology.

More on topology, Skyrmion as a topological structure can be characterized by its topological charge;

$$q = \frac{1}{4\pi} \int dx\, dy\, \mathbf{m} \cdot (\partial_x \mathbf{m} \times \partial_y \mathbf{m}) \tag{1.1}$$

with $\mathbf{m} = \mathbf{M}(\mathbf{r})/|\mathbf{M}(\mathbf{r})|$ is the unit magnetization vector. Skyrmion has topological charge $q = \pm 1$. This topological invariant is protected by the topology and is stable against weak perturbation or disorder. This topological number is preserved during the motion of the Skyrmion as long as there are no such processes as the creation or

annihilation of the Skyrmions or application of strong external field that can change the topological invariant.

1.1.3 Skyrmion Bubble

We consider thin film ferromagnet with strong perpendicular easy axis anisotropy preferring magnetization perpendicular to the plane. The particular form of topological defect we discuss in this Thesis is the so-called Skyrmion bubble. Its profile is illustrated in the following figure 1.2.

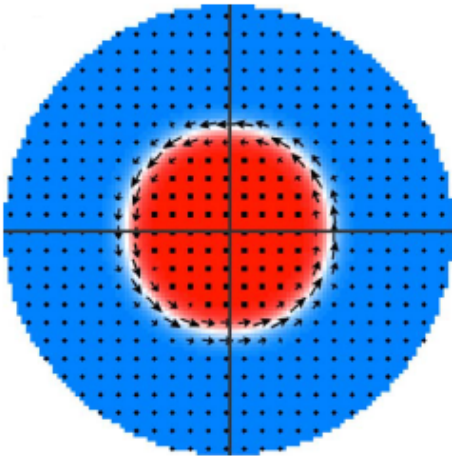

Figure 1.2: Illustration of a Skyrmion magnetic bubble [4].

Magnetization vector points into the plane (red) inside the bubble and out of the plane (blue) outside the bubble.

The bubble is defined by its boundary, which is a domain wall between the two opposite magnetization regions. Dipolar interaction makes the tension of a free magnetic bubble negative so that it has tendency to grow in size limitlessly. To prevent

this, the Skyrmion bubble is confined in a disk. In magnetic bubble Fig. 1.2, magnetization points downward inside the bubble, points in the plane at the domain wall, and point upward outside the bubble. Skyrmion in Fig. 1.1 on the other hand has magnetization point vertically downward only precisely at the center, and then the magnetization deforms slowly, pointing in the plane at some radius, and continues to slowly deform until it points upward at infinitely large distance. Despite this difference, they magnetic bubble and Skyrmion are topologically equivalent and it can be checked they both have the same topological charge defined in Eq. (1.1).

This system has been studied numerically by Moutafis *et al.* [4]. A peculiar observation is a nontrivial trajectory taken by the center of mass of the Skyrmion bubble upon application of magnetic field gradient. Previous studies of topological defects normally modeled the topological defects to be massless charged object moving under an effective magnetic field due to emergent Lorentz force, which is well expressed by Thiele's equation that can be written as (ignoring dissipation)

$$\mathbf{G} \times \dot{\mathbf{R}} + \mathbf{F} = 0 \tag{1.2}$$

where the first term is the Lorentz force and $\mathbf{F}$ is some conservative force. We find that this is not the case for a Skyrmion bubble. The most important result presented in this Thesis with regard to Skyrmion bubble dynamics is that the dynamics is described correctly if we include mass (inertia), that is, Skyrmion bubble possesses mass (inertia). We also reveal the existence of chiral edge modes on Skyrmion bubble

dynamics. This all will be described in Chapter 2.

1.2 Quantum Criticality in Pyrochlore Quantum Spin Ice

1.2.1 Frustrated Magnetism and Quantum Spin Liquid

First perceived by Phil Anderson [5], quantum spin liquid [6] [7] refers to a state without magnetic order down to absolute zero temperature. Classically, we expect any spin system to be magnetically ordered at $T = 0$ as entropy must be zero according to the third law of thermodynamics. However, quantum mechanics changes the picture as quantum fluctuations are present even at zero temperature and capable of destroying magnetic order.

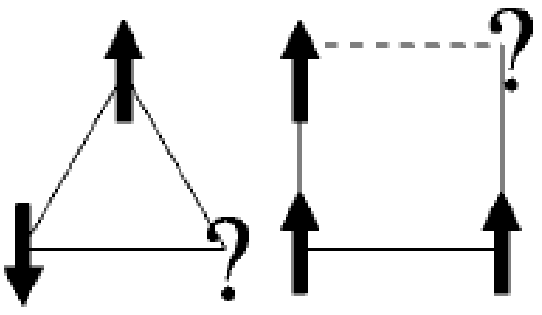

Figure 1.3: Illustration of geometric frustration of spins on a triangle with antiferromagnetic coupling and on a square with one frustrated bond [9].

In quantum magnetism, especially frustrated magnetism, geometric frustration in addition to quantum fluctuations cooperate to give rise to quantum spin liquid state. Frustration in spin systems [8] refers to the situation where the system have degenerate ground states of equal energy which frustrate the system to choose which among them to be the actual ground state. Frustration is normally caused by the geometry of the system or further neighbor interactions in a spin system. This is illustrated in Fig. 1.3. For Ising spins on a triangle with antiferromagnet coupling, one of the spins will be frustrated in deciding whether it has to be up or down. For Ising spins on square with ferromagnetic coupling on bonds with solid line and antiferromagnetic coupling on bond with dashed line, one of the spins will be frustrated.

Figure 1.4: Illustration of kagome lattice.

Kagome antiferromagnet, with 2-d corner-sharing triangle lattice in Fig. 1.4 and pyrochlore spin ice, with a 3-d corner-sharing tetrahedra lattice in Fig. 1.5, are two major candidates that could possibly host such quantum spin liquid state. Kagome

lattice contains triangles so that spins living at kagome lattice sites exhibit geometric frustration. Recent works suggest that the ground state of kagome quantum antiferromagnet is gapped Z_2 quantum spin liquid [10].

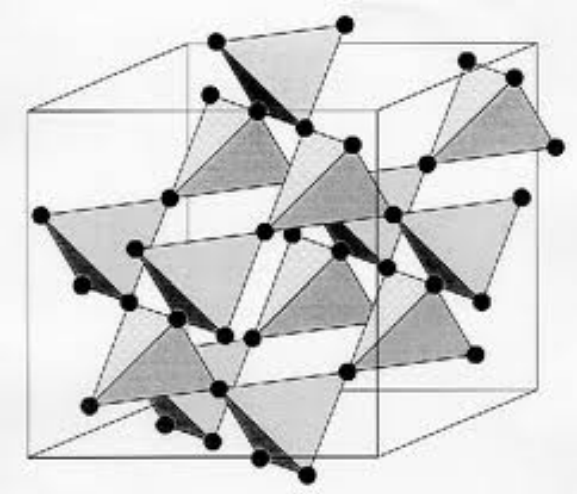

Figure 1.5: Illustration of pyrochlore lattice [19].

Pyrochlore lattice is a 3-d lattice of corner-sharing tetrahedra made up of triangles so that spins living at the sites are also frustrated with antiferromagnetic exchange. Pyrochlore quantum spin ice, to be discussed later, has long been believed to be possible host of $U(1)$ quantum spin liquid [21]. We will discuss in this Thesis the latter system.

1.2.2 Quantum Phase Transition

Quantum phase transition refers to phase transition between two different phases of matter at $T = 0$. Different from classical thermal phase transition which is driven

by changing temperature, quantum phase transition is driven by changing the parameter of the system. As is generally understood, at absolute zero, quantum phenomena play especially important role. This is also true for quantum phase transition. This topic has been very active field of research in the past few decades and it has been one field of research by itself. The first study of quantum phase transition was done by John Hertz [11] who investigated this phenomenon in itinerant ferromagnet systems and later clarified and extended by A. J. Millis [12]. The study of quantum phase transition [13] soon became more relevant with the discovery of strongly correlated electron systems such as heavy fermion and high temperature superconductors since it has been believed that quantum critical point and the corresponding quantum critical regime exist in such systems.

Nowadays, quantum phase transition is studied in various condensed matter systems including quantum magnetism. In this context, the studies are exemplified from the simplest model such as Ising model in transverse field [13] to most contemporary problems such as the transition between magnetic order and exotic spin liquid states as mentioned before [14]. It is the quantum phase transition in this is latter field which will be the focus of this Thesis. To be precise, we will discuss quantum criticality in pyrochlore quantum spin ice described in detail in Chapter 3.

1.2.3 Pyrochlore Quantum Spin Ice

Pyrochlore lattice with magnetic ions carrying spin at its sites forms pyrochlore magnet [15]. This lattice structure has been found in real materials such as $Dy_2Ti_2O_7$, $Ho_2Ti_2O_7$, $Pr_2Zr_2O_7$, and the recently actively studied $Yb_2Ti_2O_7$. Classical pyrochlore magnet has interaction between spins which is mostly long range dipolar interaction. In rare-earth materials for example, the amplitude of magnetic moments is large enough that the interaction between them is dominated by magnetic dipolar interaction [16].

$$H_D = \frac{\mu_0}{4\pi} \sum_{\mathbf{r},\mathbf{r}'} [\frac{\hat{\mathbf{m}}_\mathbf{r} \cdot \hat{\mathbf{m}}_{\mathbf{r}'}}{(\Delta r)^3} - 3\frac{(\hat{\mathbf{m}}_\mathbf{r} \cdot \Delta\mathbf{r})(\Delta\mathbf{r} \cdot \hat{\mathbf{m}}_{\mathbf{r}'})}{(\Delta r)^5}] \tag{1.3}$$

This system has been used to model classical spin ice with such Coulombic dipolar interaction [17] [18].

Recently however, it has been found that in several pyrochlore compounds, quantum effects are dominant and the interaction between spins is dominated by short range quantum spin exchange interaction. In the simplest form, it is described by Heisenberg model.

$$H = \sum_{ij} J_{ij} \mathbf{S}_i \cdot \mathbf{S}_j \tag{1.4}$$

This model has been studied classically (where the spin is treated as classical vector) to describe classical spin liquid in pyrochlore magnet [19]. When quantum fluctuations are strong and thus are important, it has been believed that pyrochlore quantum

spin ice could host exotic phases. The exotic phases of pyrochlore quantum spin ice with this short range exchange interaction manifest electrodynamics with photons, particle excitations, and Coulomb interaction between them now commonly known collectively as Coulomb phases [20] [21] which is the direct quantum analogue of classical Coulomb phase with interaction between magnetic moments given by classical dipolar interaction Eq. (1.3). The phase diagram of pyrochlore quantum spin ice modeled with more general anisotropic spin model [22] [23] has been studied theoretically "gauge mean field theory" (gMFT) which includes the gauge field fluctuations at mean field level [24]. It reveals several exotic phases consisting of $U(1)$ quantum spin liquid bordering Coulombic ferromagnet (CFM) and antiferromagnetic (AFM) phases. The first two phases have gapless photon excitations and the most interesting parts of the phase diagram.

In this Thesis a different approach to the problem by treating the gauge field explicitly is taken and a continuum field theory from the microscopic spin lattice model is derived. With the guide of gMFT phase diagram, the quantum criticality between quantum spin liquid and the neighboring magnetically ordered phases is investigated. We will study the quantum criticality of this quantum spin liquid from a gauge theory perspective where the gauge field fluctuations are treated as fully dynamical field fluctuations. The gauge theory is derived starting from the microscopic spin model followed by a spin-boson mapping formalism and further followed by continuum theory derivation to arrive at a low energy effective theory. This gauge theory

has Abelian $U(1)$ gauge structure and manifests emergent quantum electrodynamics (QED) in this frustrated spin system. A free energy description that predicts how the gauge field fluctuations modify the nature of quantum criticality of $U(1)$ quantum spin liquid with its neighboring phases in pyrochlore quantum spin ice is presented. We uncover a nontrivial quantum critical phenomenon in the form of a change in the order of phase transition driven by gauge field fluctuations. In this case, a first-order transition preempts the development of a scale-invariant state: the correlation length stays finite. The critical point however still strongly influences the phase transition since the latter is found to be weakly first-order. This all will be described in detail in Chapter 3.

Chapter 2

Dynamics of a Skyrmion Bubble in Thin Film Disk

This chapter discusses the dynamics of a Skyrmion bubble on a thin film disk. It begins with a general introduction to the problem in Section 2.1 where we emphasize the observation of new nontrivial type of dynamics in numerical simulations. In Section 2.1 we describe the phenomenological picture that can explain such dynamics. In Section 2.3, we extensively describe the micromagnetic theory of Skyrmion bubble dynamics. Numerical simulations are described in detail in Section 2.4. Part of the material presented in this chapter has been published in Phys. Rev. Lett. 109, 217201 (2012) [25].

2.1 Introduction

The dynamics of topological defects is a topic of longstanding interest in magnetism. The attention to it stems from rich basic physics as well as from its connection to technological applications [26]. The theory of magnetization dynamics in ferromagnets well below the critical temperature is based on the Landau-Lifshitz equation [27] for the unit vector of magnetization $\mathbf{m}(\mathbf{r}) = \mathbf{M}(\mathbf{r})/M$,

$$\dot{\mathbf{m}} = \gamma \mathbf{B} \times \mathbf{m} + \alpha \dot{\mathbf{m}} \times \mathbf{m} \tag{2.1}$$

where γ is the gyromagnetic ratio, α is a phenomenological damping constant [28], and the effective magnetic field is a functional derivative of the free energy, $\mathbf{B}(\mathbf{r}) = -\delta U/\delta \mathbf{M}(\mathbf{r})$. The latter includes local (e.g., exchange and anisotropy) as well as long-range (dipolar) interactions, thus making Eq. (2.1) a nonlinear and nonlocal partial differential equation with multiple length and time scales solvable in only a few simple cases. For example, translational motion of a rigid texture, $\mathbf{m} = \mathbf{m}[\mathbf{R} - \mathbf{r}(t)]$, is fully parameterized by the texture's center-of-mass $\mathbf{R}$. For steady motion, $\mathbf{R}(t) = \mathbf{V}t$, the velocity can be obtained from Thiele's equation [29] expressing the balance of gyrotropic, conservative, and viscous forces,

$$\mathbf{G} \times \dot{\mathbf{R}} + \mathbf{F} - D\dot{\mathbf{R}} = 0 \tag{2.2}$$

Here $\mathbf{G}$ is a gyrocoupling vector, $\mathbf{F} = -\delta U/\delta \mathbf{R}$ is the net conservative force, and D is a dissipation tensor.

A rigid texture moves like a massless particle with electric charge in a magnetic field and an external potential through a viscous medium. If $\mathbf{G} \neq 0$, the "Lorentz force" greatly exceeds the viscous drag. We thus ignore dissipation.

Although Eq. (2.2) was derived for steady motion, Thiele anticipated that it could serve as a good first approximation in more general situations. Indeed, his equation describes very well the dynamics of vortices in thin ferromagnetic films [30–34]. In this case, the gyrocoupling vector $\mathbf{G} = (0, 0, \mathcal{G})$ is proportional to a topological invariant known as the Skyrmion charge $q = (1/4\pi) \int dx\, dy\, \mathbf{m} \cdot (\partial_x \mathbf{m} \times \partial_y \mathbf{m})$, the film thickness t, and the density of angular momentum M/γ; to wit, $\mathcal{G} = -4\pi q t M/\gamma$. A vortex has $q = \pm 1/2$ and thus $\mathbf{G} \neq 0$. In a parabolic potential well, $U(X, Y) = \mathcal{K}(X^2 + Y^2)$, it moves in a circle at a frequency $\omega = \mathcal{K}/\mathcal{G}$.

Similar behavior is expected for other topologically nontrivial textures, e.g., magnetic bubbles in thin films with magnetization normal to the plane of the film [35] [36] [37]. A bubble is a circular domain with $m_z < 0$ surrounded by a domain with $m_z > 0$, or vice versa, Fig. 2.1 [38]. In a thin film disk with appropriate radius R, the state of lowest energy contains one circular domain wall of radius $r < R$ [39]. Recently discovered Skyrmion crystals [40] [41], particularly those which are found in thin films [42] [43], are periodic arrays of magnetic bubbles with the same Skyrmion charge $q = \pm 1$ [44]. Zang *et al.* [45] modeled Skyrmions in these structures as massless

particles with Thiele's dynamics (2.2). However, numerical simulations of Moutafis *et al.* [4] showed that this approach does not reproduce the simulated motion of an isolated bubble. In a parabolic potential, the trajectory of the bubbles center was not a circle, but "roughly a pentagon"; see Fig. 2.1.

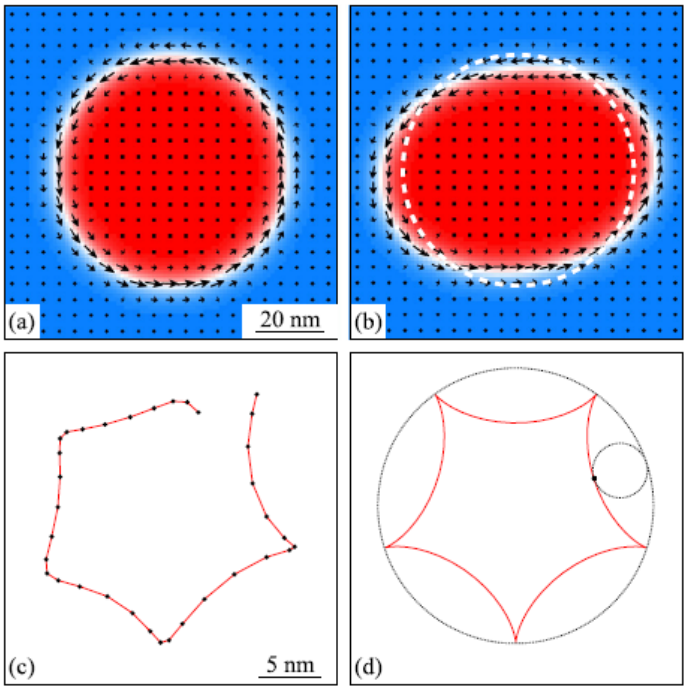

Figure 2.1: A circular magnetic bubble with Skyrmion number $q = \pm 1$. Out-of-plane magnetization is $M_z > 0$ (blue) outside the wall and $M_z < 0$ (red) inside; in-plane magnetization on the domain wall is shown by arrows. (a) Equilibrium. (b) Elliptic deformation. The dashed line marks the equilibrium position of the domain wall. (c) The trajectory of the bubble's center observed by Moutafis *et al.* [4] Dots mark positions evenly spaced in time. (d) A 5-cusped hypocycloid with its directing and generating circles.

2.2 Phenomenological Picture

The puzzling trajectory of the bubbles center is readily reproduced if we endow a Skyrmion bubble with inertial mass $\mathcal{M}$,

$$-\mathcal{M}\ddot{\mathbf{R}} + \mathbf{G} \times \dot{\mathbf{R}} - \mathcal{K}\mathbf{R} = 0 \tag{2.3}$$

In component form, for topological defect moving on two dimensional $x - y$ plane, the equation above takes the form

$$\mathcal{M}\ddot{X} - \mathcal{G}\dot{Y} - \mathcal{K}X = 0$$

$$\mathcal{M}\ddot{Y} + \mathcal{G}\dot{X} - \mathcal{K}Y = 0$$

When combined, the new equation of motion is of the second order in d/dt and has two circular modes with frequencies,

$$\omega_{\pm} = -\mathcal{G}/(2\mathcal{M}) \pm \sqrt{(\mathcal{G}/(2\mathcal{M}))^2 + \mathcal{K}/\mathcal{M}} \tag{2.4}$$

In the limit of $\mathcal{M} \to 0$, we have

$$\begin{aligned}\omega_{\pm} &= -\frac{\mathcal{G}}{2\mathcal{M}} \pm \frac{\mathcal{G}}{2\mathcal{M}}\sqrt{1 + \frac{4\mathcal{M}\mathcal{K}}{\mathcal{G}^2}} \\ &\simeq -\frac{\mathcal{G}}{2\mathcal{M}} \pm \frac{\mathcal{G}}{2\mathcal{M}}\left(1 + \frac{2\mathcal{M}\mathcal{K}}{\mathcal{G}^2}\right)\end{aligned}$$

which gives $\omega = \mathcal{K}/\mathcal{G}$ for one of the modes. This agrees with Thiele's result which treats Skyrmion bubble as massless charged object, but the result of numerics [4]

suggests the presence of two modes, which is made possible by the nonzero mass term in Eq. (2.3).

Given the two frequencies in Eq. (2.4), a particle with zero initial velocity follows a hypocycloid. If $\omega_-/\omega_+ = -4$, the hypocycloid has five cusps and indeed resembles a pentagon, Fig. 2.1. We repeated the simulations of Moutafis *et al.* [4] and found that the motion of the bubble is described with good accuracy by a superposition of two underdamped modes with eigenfrequencies $\omega/2\pi = 0.97$ GHz and $\omega/2\pi = -4.27$ GHz.

2.3 Theory of the Dynamics of a Skyrmion Bubble

To understand the origin of inertia, we shift attention from the center of the bubble, where nothing is happening, to its boundary, a domain wall defined as a line $y(x)$, where $M_z(x, y) = 0$. A nearly circular domain wall is conveniently parameterized in polar coordinates

$$r(\phi) = \overline{r} + \sum_m r_m e^{im\phi} \tag{2.5}$$

The Fourier amplitudes $r_m = r^*_{-m}$ describe waves with wave numbers $k = m/\overline{r}$ traveling along the circular edge: r_0 is the breathing mode, $r_1 = (X - iY)/2$ encodes the location of the center of mass, r_2 parameterizes elliptical deformations, Fig. 2.1,

and so on. On the domain wall, magnetization lies in the plane of the film, $\mathbf{m} = (\cos\psi, \sin\psi, 0)$. For a circular wall in equilibrium, $\mathbf{m}$ points along the direction of the wall, $\psi = \phi \pm \pi/2$, Fig. 2.1. More generally,

$$\psi(\phi) = \phi \pm \pi/2 + \sum_m \psi_m e^{im\phi} \tag{2.6}$$

The fields $r(\phi)$ and $\psi(\phi)$ are coupled to each other, and so are their harmonics r_m and ψ_m. Integrating out ψ_1 generates kinetic energy for the center of mass.

We derive the dynamics of transverse fluctuations of a Bloch domain wall, first for a straight wall and then for a circular one. To this end, we employ a method of collective coordinates generalizing Thiele's approach beyond steady motion [46]. The Lagrangian formalism allows us to easily integrate out the hidden degree of freedom—in-plane magnetization—in favor of the more evident transverse motion. An evolving magnetic texture $\mathbf{m}(\mathbf{r}, t)$ can be parameterized by a (potentially infinite) set of collective coordinates $\xi(t) = (\xi_1(t), \xi_2(t), \ldots)$. Their equations of motion are similar to Thiele's equation (2.2),

$$G_{ij}\dot{\xi}_j + F_i - D_{ij}\dot{\xi}_j = 0 \tag{2.7}$$

with generalized forces $F_i = -\partial U/\partial \xi_i$, gyrotropic coefficients G_{ij}, and viscosity coefficients D_{ij}. Both G_{ij} and D_{ij} are second rank tensor satisfying $G_{ij} = -G_{ji}$ and $D_{ij} = D_{ji}$ respectively. To be precise, they are given by

$$D_{ij} = \alpha J \int dV \, \frac{\partial \mathbf{m}}{\partial \xi_i} \cdot \frac{\partial \mathbf{m}}{\partial \xi_j} \tag{2.8}$$

$$G_{ij} = J \int dV \, \mathbf{m} \cdot \left(\frac{\partial \mathbf{m}}{\partial \xi_i} \times \frac{\partial \mathbf{m}}{\partial \xi_j} \right) \tag{2.9}$$

where $J = M/\gamma$ (M is the saturation magnetization, γ is gyrotropic ratio) is the angular momentum density.

Equation (2.7) can be derived directly from Landau-Lifshitz-Gilbert equation (2.1) as has been done in Ref. [46]. Equation (2.7) can also be obtained from a Lagrangian $L = \mathbf{A} \cdot \dot{\xi} - U(\xi)$, where $\mathbf{A}(\xi)$ is a gauge potential with curvature $\partial A_j/\partial \xi_i - \partial A_i/\partial \xi_j = G_{ij}$ [47]. The gauge term contributes to the action $S = \int L dt$ a time-independent piece $\int \mathbf{A} \cdot d\xi$ known as Berry's geometric phase.

2.3.1 Energy Components of a Skyrmion Bubble

In general, the most important energy components of ferromagnet consist of exchange, anisotropy, Zeeman, and magnetostatic. Exchange energy describes the energy cost of creating nonuniform magnetization pattern. Uniform magnetization pattern therefore minimizes exchange energy. Anisotropy energy describes the energy cost of creating magnetization pattern away from certain easy axis or easy plane. Anisotropy energy is minimized when the magnetization is oriented along easy axis or on an easy plane. Zeeman energy is the usual coupling energy between magnetization and external magnetic field. The above mentioned forms of energy are local in

nature. Finally, magnetostatic energy is the intrinsic energy of magnetic field.

In any sample, the magnetostatic energy can be written as Coulombic dipolar interaction between effective magnetic charges. The effective magnetic charges represent the physical effects of magnetization and in this context consist of bulk (volume) charge and surface charge in the most general case. Volume charge density is given by $\rho = -\nabla \cdot \mathbf{M}$ whilst surface charge density is given by $\sigma = \mathbf{M} \cdot \hat{\mathbf{n}}$. These charges contribute to both local and nonlocal energy components of domain wall. This dipolar interaction leads to the tendency to form domains of opposite magnetization separated by domain wall rather than a single domain of uniform magnetization preferred by exchange interaction. It will be shown later that dipolar interaction leads to negative tension for domain wall which makes it tend to grow larger indefinitely unless it is constrained by a confining geometry. In this Thesis, all these energy components will be calculated explicitly in detail and they constitute a micromagnetic description of Skyrmion bubble in thin film ferromagnet and determine the nature of its dynamics. We will first analyze the dynamics using Lagrangian formalism, starting with the straight domain wall approximation before considering the actual Skyrmion bubble problem.

2.3.2 Straight Domain Wall Approximation

We first consider the dynamics of a domain wall stretched along the x axis, $y(x,t) \approx 0, \psi(x,t) \approx 0$, from $x = 0$ to $x = l$. Its Lagrangian,

$$L[y,\psi] = \int_0^l dx\, g\dot{y}\psi - U[y,\psi] \tag{2.10}$$

contains a gauge term with gyrotropic coupling $g = 2tM/\gamma$ [48] [49]. The resulting equations of motion are $-g\dot{\psi} - \delta U/\delta y = 0, g\dot{y} - \delta U/\delta\psi = 0$ in the absence of dissipation. The in-plane magnetization is aligned with the wall in equilibrium, $\psi = y' = \partial y/\partial x$; the cost of small misalignments is quadratic in $\psi - y'$, so

$$L[y,\psi] = \int_0^l dx\, [g\dot{y}\psi - \kappa(\psi - y')^2/2] - U[y] \tag{2.11}$$

with the stiffness κ is to be determined. The field ψ can be integrated out with the aid of its equation of motion, $g\dot{y} - \kappa(\psi - y') = 0$, to obtain a Lagrangian for transverse displacement

$$L[y] = \int_0^l dx\, (g\dot{y}y' + \rho\dot{y}^2/2) - U[y] \tag{2.12}$$

where $\rho = g^2/\kappa$ is the Döring mass density [48] [49]. Potential energy of a domain wall can be split into local and long-range contributions. The local term is proportional to the length of the wall and tension

$$U_l[y] = \int_0^l dx\, \sigma\sqrt{dx^2 + dy^2} \approx U_l[0] + \int_0^l dx\, \sigma y'^2/2 \tag{2.13}$$

where $U_l[0] = \sigma l$ is the energy of a straight wall. Thus,

$$L[y] = \int dx \, (\rho \dot{y}^2/2 + g\dot{y}y' - \sigma y'^2/2) - U_{nl}[y] \tag{2.14}$$

Neglecting for the moment the nonlocal term $U_{nl}[y]$, we obtain a wave equation, $\rho\ddot{y} + 2g\dot{y}' - \sigma y'' = 0$, with waves traveling left and right at different speeds, cf. Eq. (2.4),

$$\omega = \rho^{-1}(-gk \pm \sqrt{g^2k^2 + \sigma\rho k^2}) \tag{2.15}$$

In the limit $\sigma \ll g^2/\rho = \kappa$, the slow wave has velocity $v_1 \sim \sigma/2g$ that is insensitive to inertia; in-plane magnetization adiabatically aligns with the direction of the wall. The fast mode with velocity $v_2 \sim -2g/\rho$ involves oscillations of in-plane magnetization out of phase with those of the direction of the wall.

A minimal model of a thin-film ferromagnet with out-of plane magnetization includes exchange coupling A and easy-axis anisotropy K strong enough to overcome the dipolar shape anisotropy: the "quality factor" $Q = 2K/\mu_0 M^2$ must exceed 1. In this model, a domain wall has the width $\lambda/\sqrt{Q-1}$, where $\lambda = \sqrt{2A/\mu_0 M^2}$ is the exchange length, and tension $\sigma = 2\mu_0 M^2 t\lambda\sqrt{Q-1}$. The coupling between the in-plane magnetization and the direction of the wall is $\kappa = \sigma/(Q-1)$. By using the material parameters characteristic of FePt with thickness $t = 32$ nm [4], we obtain $v_1 = 370$ m/s and $v_2 = -2100$ m/s in the local model.

The nonlocal part of the potential energy comes from long-range dipolar interactions. A domain wall in a thin ferromagnetic film produces a stray magnetic field

whose energy can be written as a double line integral along the domain wall [50] [51],

$$U_{nl}[\mathbf{r}] = -\frac{\sigma_d}{2}\int \frac{d\mathbf{r}_1 \cdot d\mathbf{r}_2}{|\mathbf{r}_1 - \mathbf{r}_2|} \tag{2.16}$$

where $\sigma_d = \mu_0 M^2 t^2/\pi$ is "dipolar tension". This expression diverges at both short and long length scales and thus requires both short- and long-distance cutoffs (provided by the film thickness and the wall length). The local potential energy (2.13) may be absorbed into the nonlocal part (2.16) at the expense of renormalizing the short-distance cutoff. Expanding Eq. (2.16) to the second order in y yields the following result:

$$U_{nl}[y] = U_{nl}[0] + l\int_0^\infty \frac{dk}{2\pi}\,\sigma_d k^2 \ln(ka)|y_k|^2 \tag{2.17}$$

where $y_k = l^{-1/2}\int_0^l dx\, y(x)e^{-ikx}, U_{nl}[0] \sim -\sigma_d l \ln(l/a)$ is the energy of a straight domain wall coming from the nonlocal long range dipolar interaction, $a = (t/2)\, e^{C-1+\sigma/\sigma_d}$ is a short-distance length scale, and $C = 0.577...$ is the Euler constant. The wave stiffness $\sigma_d k^2 \ln(ka)$ is negative for $k < 1/a$, which means that a straight domain wall is unstable against small deformations. This is the fingering instability occurring in systems with long-range interactions [50] [52]. It can be prevented by placing the domain wall in a strip of finite width w. Repulsion from the edges, mediated by a stray magnetic field, increases the wave stiffness by a k-independent term $4\sigma_d/w^2$. The wave frequencies are

$$\omega = \rho^{-1}[-gk \pm \sqrt{g^2k^2 + \sigma_d\rho(k^2 \ln|ka| + 4/w^2)}] \tag{2.18}$$

The frequency spectrum (Fig. 2) has two significant changes from the local model (2.15): a gap opens up; the band bottom is shifted to $k_0 = e^{1/2}a^{-1}$.

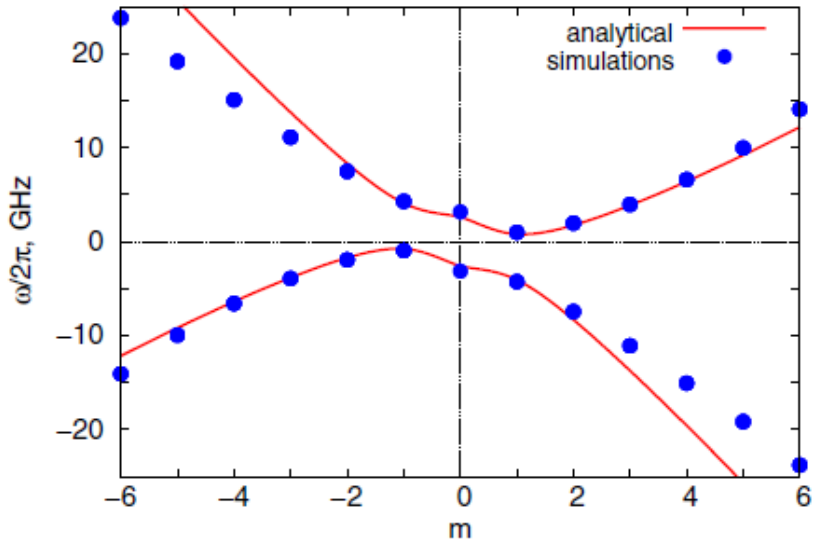

Figure 2.2: The spectrum of spin waves $\omega/2\pi$ on a circular domain wall: Numerical simulation (circles), model calculations for a straight wall (2.18) with $k = m/\overline{r}$ (line).

In the following segment, we give the details of the calculation of local and nonlocal interactions.

2.3.2.1 Local Interaction

Tension σ and alignment stiffness κ come from the local portion of the energy functional. Consider a ferromagnetic film of thickness t with two domains of mag-

netization, $\mathbf{m} = (0, 0, 1)$ and $\mathbf{m} = (0, 0, -1)$, separated by a straight domain wall of length l along the x-axis. The magnetization field can be parameterized as

$$\mathbf{m}(y) = (\sin\theta\cos\phi, \sin\theta\sin\phi, \cos\theta) \tag{2.19}$$

with $\theta = \theta(y)$ and $\phi = \text{const}$. In the state of lowest energy, in-plane magnetization points along the wall, $\phi = 0$ (Bloch wall) as shown in Fig. 2.3.

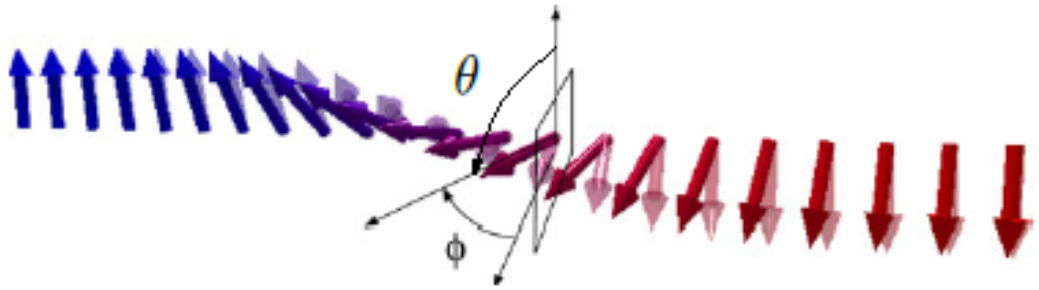

Figure 2.3: Bloch wall configuration.

The energy contains three terms: exchange energy

$$U_{\text{exchange}} = At \int d^2r\ (\partial_i \mathbf{m}) \cdot (\partial_i \mathbf{m}) = Atl \int_{-\infty}^{\infty} dy \left(\frac{d\theta}{dy}\right)^2,$$

easy-axis anisotropy

$$U_{\text{anisotropy}} = -Kt \int d^2r\, m_z^2 = -Ktl \int_{-\infty}^{\infty} dy\, \cos^2\theta,$$

and the energy of the magnetic field, which can be evaluated as the Coulomb interaction of magnetic charges at the top and bottom surfaces of the film with area

densities $\mp M_z(\mathbf{r})$:

$$U_{\text{dipolar}} = \frac{\mu_0}{4\pi} \int d^2r_1 d^2r_2 \, V(\mathbf{r}_1 - \mathbf{r}_2) M_z(\mathbf{r}_1) M_z(\mathbf{r}_2) \tag{2.20}$$

with the interaction kernel

$$V(\mathbf{r}) = \frac{1}{r} - \frac{1}{\sqrt{r^2 + t^2}} \equiv \mathbb{V}(r) \tag{2.21}$$

For future convenience, we extend the definition of $\mathbb{V}(x)$ to negative values of the argument so that $\mathbb{V}(-x) = \mathbb{V}(x)$:

$$\mathbb{V}(x) = \frac{1}{|x|} - \frac{1}{\sqrt{x^2 + t^2}} = \lim_{\epsilon \to 0} \frac{1}{\sqrt{x^2 + \epsilon^2}} - \frac{1}{\sqrt{x^2 + t^2}} \tag{2.22}$$

The interaction kernel $V(\mathbf{r})$ has a peak with a characteristic width of the order of the film thickness t. If magnetization varies slowly on that length scale, we may approximate $V(\mathbf{r}) \approx 2\pi t \delta(\mathbf{r})$. Then the dipolar energy assumes a local form:

$$U_{\text{dipolar}} \approx t \int d^2r \, \frac{\mu_0 M_z^2}{2} = \frac{\mu_0 M^2 t l}{2} \int_{-\infty}^{\infty} dy \, \cos^2\theta \tag{2.23}$$

Put another way, we make a local approximation for the magnetic field inside the film, $H_z(\mathbf{r}) \approx -M_z(\mathbf{r})$, whose energy density $\mu_0 H^2/2 \approx \mu_0 M_z^2/2$.

The energy cost of a domain wall is thus

$$U = lt \int_{-\infty}^{\infty} dy \, [A\theta'^2 + (K - \mu_0 M^2/2) \sin^2\theta] \tag{2.24}$$

Minimization of this energy yields the domain-wall profile

$$\cos\theta\,(y) = \tanh\left(\frac{y}{\lambda}\sqrt{Q-1}\right) \tag{2.25}$$

where $\lambda = \sqrt{2A/\mu_0 M^2}$ is the exchange length and $Q = 2K/\mu_0 M^2 > 1$ is the "quality factor". The minimized energy per unit length gives line tension

$$\sigma = U/l = 2\mu_0 M^2 t\lambda\sqrt{Q-1} \tag{2.26}$$

When in-plane magnetization deviates from the direction of the wall, it creates bulk magnetic charges with volume density $-\nabla\cdot\mathbf{M} = -dM_y/dy$. This induces an additional magnetic field $H_y \approx -M_y$ and thus generates additional energy density $\mu_0 H_y^2 \approx (\mu_0 M^2/2)\sin^2\theta\sin^2\psi$. The domain-wall energy per unit length increases to

$$U(\psi)/l = 2\mu_0 M^2 t\lambda\sqrt{Q-1+\sin^2\psi} \sim \sigma + \kappa\psi^2/2 \tag{2.27}$$

for small angles ψ. The strength of coupling between the azimuthal angle and the direction of the wall is

$$\kappa = \frac{1}{l}\left.\frac{d^2U}{d\psi^2}\right|_{\psi=0} = \frac{\sigma}{Q-1} \tag{2.28}$$

2.3.2.2 Long-range Interaction

Equation (2.23) captures the local part of dipolar energy, whose density is determined by the local value of magnetization. Inhomogeneities in magnetization produce a stray magnetic field that gives rise to a nonlocal component,

$$U_{\text{stray}} = \frac{\mu_0}{4\pi} \int d^2 r_1 d^2 r_2 \, G(\mathbf{r}_1 - \mathbf{r}_2) \nabla M_z(\mathbf{r}_1) \cdot \nabla M_z(\mathbf{r}_2); \tag{2.29}$$

where $\mathbf{r} = (x, y)$ and $\nabla = (\partial_x, \partial_y)$ are two-dimensional vectors. The kernel is defined as a solution to the equation $\nabla^2 G(\mathbf{r}) = -V(\mathbf{r})$ and has the explicit form

$$G(\mathbf{r}) = \sqrt{r^2 + t^2} - r - t \operatorname{arcsinh}(t/r) \equiv \mathbb{G}(\mathbf{r}) \tag{2.30}$$

As we did for $\mathbb{V}(x)$, we extend the definition of $\mathbb{G}(x)$ to $x < 0$ so that $\mathbb{G}(-x) = \mathbb{G}(x)$. Note that

$$\mathbb{G}''(x) + \mathbb{G}(x)/x = -\mathbb{V}(x) \tag{2.31}$$

For an infinitely sharp domain wall, Eq. (2.29) reduces to a double line integral,

$$U_{\text{stray}}[\mathbf{r}] = \frac{\mu_0 M^2}{\pi} \int d\mathbf{r}_1 \cdot d\mathbf{r}_2 \, G(\mathbf{r}_1 - \mathbf{r}_2) \tag{2.32}$$

The asymptotic form of the kernel (2.30) is $G(\mathbf{r}) \sim -t^2/r$ for $r \gg t$. Hence

$$U_{\text{stray}}[\mathbf{r}] \approx -\frac{\sigma_d}{2} \int \frac{d\mathbf{r}_1 \cdot d\mathbf{r}_2}{|\mathbf{r}_1 - \mathbf{r}_2|} \tag{2.33}$$

with "dipolar tension"

$$\sigma_d = \frac{\mu_0 M^2 t^2}{\pi} \tag{2.34}$$

The simplified version of the stray-field interaction (2.32) is logarithmically divergent at short distances. One way to handle the divergence is to impose a short- distance cutoff, $|\mathbf{r}_1 - \mathbf{r}_2| > b$, where b is a length scale of the order of the film thickness t. The energy of a straight wall due to its stray field, computed with the exact expression (2.30), is

$$U_{\text{stray}} \sim -\sigma_d l \left[\ln(2l/t) + 1/2\right] \tag{2.35}$$

whereas the simplified version (2.32) with a cutoff yields

$$U_{\text{stray}} \sim -\sigma_d l[\ln(l/b) - 1] \tag{2.36}$$

The two expressions agree if we choose cutoff to be

$$b = (t/2)e^{-3/2} \tag{2.37}$$

Local contributions to the energy of the domain wall σl can be absorbed into the stray-field energy (2.36) at the expense of renormalizing the cutoff parameter,

$$b = (t/2)e^{-3/2+\sigma/\sigma_d} \tag{2.38}$$

2.3.2.3 Energy of transverse fluctuations

We compute the energy of a nearly straight domain wall, $y(x) \approx 0$. The local part can be written as

$$U_{\rm loc}[y] = \int_0^l dx\, \frac{\sigma}{2} y'^2 = l \int_0^\infty \frac{dk}{2\pi}\, \sigma k^2 |y_k|^2 \tag{2.39}$$

where $y_k = l^{-1/2} \int_0^l dx\, y(x) e^{-ikx}$ is the spatial Fourier transform of $y(x)$.

The energy of the stray field (2.32) can be expanded to $\mathcal{O}(y^2)$ with the aid of the following results:

$$d\mathbf{r}_1 \cdot d\mathbf{r}_2 = dx_1 dx_2\, [1 + y'(x_1) y'(x_2)],$$

$$G(\mathbf{r}) = \mathbb{G}(\sqrt{x^2 + y^2}) = \mathbb{G}(x) + \mathbb{G}'(x) y^2/2x + \mathcal{O}(y^4).$$

The nonlocal portion of the energy of transverse fluctuations thus consists of two parts,

$$U_{\rm stray}[y] = \frac{\mu_0 M^2}{\pi} \int dx_1 dx_2\, \mathbb{G}(x_1 - x_2) y'(x_1) y'(x_2) + \frac{\mu_0 M^2}{\pi} \int dx_1 dx_2\, \frac{\mathbb{G}'(x_1 - x_2)}{2(x_1 - x_2)} (y_1 - y_2)^2.$$

After an integration by parts and a Fourier transform, we obtain

$$U_{\rm stray}[y] = l \int_0^\infty \frac{dk}{2\pi}\, A_k |y_k|^2, \tag{2.40}$$

where

$$A_k = \frac{2\mu_0 M^2}{\pi} \int_{-\infty}^{\infty} dx \, [1 - \cos(kx)][\mathbb{G}''(x) + \mathbb{G}'(x)/x]$$

With the aid of Eqs. (2.22) and (2.31), we obtain

$$A_k = -\frac{4\mu_0 M^2}{\pi} \, [K_0(kt) + \ln(kt/2) + C] \tag{2.41}$$

where $K_0(x)$ is a modified Bessel function and $C = 0.577...$ is the Euler constant. In the infrared limit, $kt \to 0$,

$$A_k \sim \sigma_d k^2 [\ln(kt/2) + C - 1].$$

Upon adding the local term (2.39), we obtain

$$U[y] \sim l \int_0^{\infty} \frac{dk}{2\pi} \sigma_d \, k^2 \ln(ka) |y_k|^2 \tag{2.42}$$

with the short-distance scale

$$a = (t/2) e^{C-1+\sigma/\sigma_d} \tag{2.43}$$

2.3.3 The Peculiar Physics of Dipolar Interaction

In the course of deriving this rigorous analytical treatment of Skyrmion bubble dynamics, we encounter a very interesting subtlety which carries important message and lesson on the physics of dipolar interaction, as it affects the Skyrmion bubble

dynamics. In computing the wall-wall dipolar energy Eq. (2.71), we have to impose short distance cutoff, in order to handle the singularity in the integral. We determine this cutoff by comparing the exact expression for straight domain wall self dipolar energy arising from the stray field. This is done by comparing the energy expression from exact kernel (with exact Green's function for dipolar interaction; the long range Coulomb interaction in two dimensions) and the energy expression using approximate kernel, with that short distance cutoff which we are looking for. We have done this in subsection 2.3.1 and obtained $a = (t/2)\exp(-3/2)$ as we stated just after Eq. (2.36). The calculation in that subsection can be considered to be short distance cutoff calculation based on the energy of a static domain wall.

To check the correctness of the result, we also compute the short distance cutoff from the energy dispersion of dynamical nearly straight domain wall in a strip. The local components of the energy have been computed in the previous subsection and since UV divergence which demands short distance cutoff only appears in self dipolar energy, we proceed directly to compute the long-ranged dipolar interaction energy. For a straight domain wall in a strip, this energy consists of dipolar interaction between the wall and itself, here referred to as $U_{\text{stray}}^{\text{wall-wall}}$ and the interaction between the wall and the edge of the strip, here referred to as $U_{\text{stray}}^{\text{wall-edge}}$ which are written as follows,

$$U_{\text{stray}}^{\text{wall-wall}} = -\frac{\Omega}{2\pi}\int\int \frac{d\mathbf{r}\cdot d\mathbf{r}'}{|\mathbf{r}-\mathbf{r}'|} \tag{2.44}$$

and

$$U_{\text{stray}}^{\text{wall-edge}} = +\frac{\Omega}{4\pi}\int\int \frac{d\mathbf{r}\cdot d\mathbf{r}'}{\sqrt{(x-x')^2+(y\pm\frac{w}{2})^2}} \tag{2.45}$$

where $\Omega = \mu_0 M^2 t^2$. The calculation proceeds with expanding the denominator in each expression in terms of appropriate small expansion parameter which is valid for the nearly-straight domain wall case and retaining the lowest (up to quadratic) order contributions. The total potential energy including these long-ranged nonlocal dipolar contributions will take the form

$$E = \sigma L + \int_{-\infty}^{\infty} \frac{dk}{2\pi}\varepsilon_k |y_k|^2 \tag{2.46}$$

where the energy dispersion is given by

$$\varepsilon_k = \frac{2\Omega}{\pi w^2} + \frac{\sigma_d}{2}\left[C + \frac{3}{2} + \ln(ka)\right]k^2 + \frac{1}{2}\sigma k^2 \tag{2.47}$$

where $\sigma_d = \Omega/\pi = \mu_0 M^2 t^2/\pi$, and $C = 0.577$ is the Euler-Mascheroni number and w is the width of the strip. In this result we have to introduce short distance (UV) cutoff a because we used approximate kernel.

An alternative approach which can directly give the actual value of the short-distance cutoff naturally is by computing the long-ranged dipolar energy explicitly using the exact kernel for two-dimensional dipolar interaction. We also have done this in the previous subsection in the calculation of energy of transverse fluctuations. Combining with the local and wall-edge stray field energy, the net result is

$$E = \int_{-\infty}^{\infty} \frac{dk}{2\pi} \epsilon_k |y_k|^2 \tag{2.48}$$

where

$$\epsilon_k = \frac{2\Omega}{\pi w^2} + \frac{\sigma_d k^2}{2} \left[-1 + C + \ln\left(\frac{kt}{2}\right) \right] + \frac{\sigma k^2}{2} \tag{2.49}$$

Direct comparison with Eq. (2.47) suggests that in computing dipolar energy using approximate kernel through lowest order expansion of the exact kernel, the unknown short distance cutoff a must be set to $a = (t/2)\exp(-5/2)$. We see that we have obtained new value of short distance cutoff, different from the result derived earlier in Eq. (2.37). Natural question arises, which one is the right short distance cutoff?

This issue reflects the peculiarity and subtlety of dipolar interaction, something which is a very delicate issue and has been hardly emphasized in the literature (from more physical rather than mathematical perspective, which has been discussed by, e.g. [50] in other context) regarding the singularity of dipolar interaction. The lesson that we learn from this finding is that, dipolar interaction not only has troublesome long distance properties as it is long-ranged and is therefore singular (it has $\sim 1/k^2$ singularity in Fourier space giving rise to $V(\mathbf{r}) \sim 1/|\mathbf{r}|$ in 3-d and $V(\mathbf{r}) \sim \ln|\mathbf{r}|$ in 2-d), but also has troublesome short distance properties. It behaves badly both on long and short length scales. A cavalier handling of the short-range cutoff in this case sometimes leads to inconsistent answers, so there is indeed sensitivity to the microscopic details in this problem. We find above that the dipolar energy can be

computed approximately but it involves short distance cutoff that has not so well defined value as it depends on the specific way we compute the cutoff. To be precise, it depends on the specific regularization procedure; the procedure that we use to regularize the short distance singularity of the dipolar self energy. This bears some similarity with regularization method in quantum field theory where one can take any scheme to regularize the ultraviolet (short distance, high energy) singularity of electron self energy in QED for example, and the value of self energy, which is not physical, in general depends on the regularization scheme being used (hard cutoff, Pauli-Villar etc. regularization scheme), but the final results in terms of physically measurable properties should not depend on the regularization scheme; that is, all different regularization scheme must give the same final answer for experimentally measurable properties.

2.3.4 Dynamics of a Skyrmion Bubble

The dynamics of a circular domain wall is derived along similar lines. For a wall of given shape (2.5), the in-plane magnetization tends to align itself with the wall, $\psi_{eq}(\phi) = \phi \pm \pi/2 - \overline{r}^{-1}\partial r/\partial\phi$. The ψ-dependent terms in the Lagrangian density are thus $g\dot{r}\psi - \kappa(\psi - \psi_{eq})^2/2$. The Lagrangian of the Fourier modes (2.5) and (2.6) is

$$L[r,\psi] = 2\pi\overline{r}\sum_m \left(g\dot{r}_m\psi_m^* - \frac{\kappa|\psi_m + imr_m/\overline{r}|^2}{2} \right) - U[r] \tag{2.50}$$

Integrating out ψ yields a Lagrangian for r containing both kinetic energy and a Berry-phase term,

$$L[r] = \sum_m \left(\pi \overline{r} \rho |\dot{r}_m|^2 - 4\pi m i g r_m^* \dot{r}_m\right) - U[r] \tag{2.51}$$

We thus arrive at a Lagrangian for the center-of-mass mode $r_1 = (X - iY)/2$,

$$L(X, Y) = \mathcal{M}(\dot{X}^2 + \dot{Y}^2)/2 + \mathcal{G}\dot{X}Y - \mathcal{K}(X^2 + Y^2)/2. \tag{2.52}$$

It yields the anticipated inertial dynamics of a magnetic bubble (2.3). The gyrotropic constant, $\mathcal{G} = 2\pi g = 4\pi t M/\gamma = 2.29 \times 10^{-12}$J s/m^2, depends only on the topology of the bubble (here the Skyrmion number $q = 1$) and on the area density of angular momentum tM/γ; therefore, it can be taken at face value. The spring constant $\mathcal{K}$ comes from magnetostatic repulsion between the domain wall and the edge of the disk; its calculated value, $\mathcal{K}_{\text{calc}} = 0.020$ J/m^2 for $\overline{r} = 37$ nm, should also be reliable. The basic constant $\mathcal{G}$ can be combined with the measured frequencies, $\omega_{\text{sim}}/2\pi = 0.97$ GHz and -4.27 GHz, to obtain $\mathcal{K}_{\text{sim}} = 0.018$ J/m^2. We note that we find good match between the calculated and simulated values of the spring constant $\mathcal{K}$.

In the following subsections, we present a rigorous treatment of Skyrmion bubble dynamics. We do so in order to demonstrate how good our theory in its more rigorous form beyond nearly straight domain wall approximation can reproduce and explain the numerical result on the actual Skyrmion bubble.

2.3.4.1 Skyrmion Bubble in Equilibrium

Magnetization in a ferromagnet well below its Curie point has a fixed magnitude M. We will use similar parameterization as used in Eq. (2.19) but now applied to polar coordinate appropriate for thin film disk $\theta = \theta(\mathbf{r}), \phi = \phi(\mathbf{r})$. Similar to the nearly straight domain wall case, the total energy consists of exchange, anisotropy, and dipolar energy. The local part of these energies will just be proportional to the wall length; the circumference of the Skyrmion bubble. The stray field consists of the wall-wall stray field U_{stray1} and the wall-edge stray field U_{stray2}, just like those of nearly straight domain wall on a narrow strip, with the edge being that of the disk in this case. On top of that, since we study the dynamics of a Skyrmion bubble under nonuniform magnetic field $\mathbf{H}_{\text{ext}} = (0, 0, g_x x + g_y y)$ with magnetic field gradient $\mathbf{g} = (g_x, g_y)$ following [4], there is also the crucial Zeeman energy which can be expressed as

$$U_{\text{Zeeman}} = 2\mu_0 M t \mathcal{A}\, \mathbf{r}_c \cdot \mathbf{g} \tag{2.53}$$

where $\mathcal{A} = \int d^2r$ is the area inside the domain wall and $\mathbf{r}_c = (1/\mathcal{A}) \int d^2r\, \mathbf{r}$ its center of mass. This result, which assumes that $M_z = -M$ inside the domain wall, can be derived by noting that $1 - \cos\theta = 2$ inside the wall and 0 outside:

$$U_{\text{Zeeman}} = \mu_0 M \int d^2r\, (\mathbf{g} \cdot \mathbf{r}) \cos\theta = \text{const} + \mu_0 M \int d^2r\, (\mathbf{g} \cdot \mathbf{r})(1 - \cos\theta)$$

$$= \text{const} + 2\mu_0 M t \mathcal{A}\, \mathbf{r}_c \cdot \mathbf{g} \tag{2.54}$$

In the absence of the field gradient $\mathbf{g}$, the wall is circular and concentric with the disk. To find the equilibrium radius of the wall $\overline{r}$, we evaluate the local and stray terms for a wall of constant radius and minimize the total energy with respect to $\overline{r}$:

$$U_{\text{local}} = 2\pi\sigma\overline{r} \tag{2.55}$$

$$U_{\text{stray1}} = -2\overline{r}[\ln(4\overline{r}/a) - 2] \tag{2.56}$$

where $a = (t/2)\exp(-3/2)$.

$$U_{\text{stray2}} = 2\Omega\sqrt{R\overline{r}} \int_0^{\pi/2} d\phi\, \frac{1 - 2\sin^2\phi}{\sqrt{\epsilon^2 + \sin^2\phi}} \tag{2.57}$$

where $\epsilon^2 = (R-\overline{r})^2/(4R\overline{r})$. The last line can be reduced to complete elliptic integrals $K(k)$ and $E(k)$ with the complementary modulus $k' = \sqrt{1-k^2} = (R-\overline{r})/(R+\overline{r})$:

$$U_{\text{stray2}} = 2\Omega(R+\overline{r})\left(\frac{R^2+\overline{r}^2}{(R+\overline{r})^2}K(k) - E(k)\right) \tag{2.58}$$

The total potential energy $U = U_{\text{local}} + U_{\text{stray1}} + U_{\text{stray2}}$ has the profile as function of average radius $\overline{r}$ shown in Fig. 2.4, which shows that there is a local minimum at $\overline{r} \simeq 41$ nm which agrees very well with the result of Ref. [4] where $\overline{r} \simeq 37$ nm.

When the field gradient $\mathbf{g}$ is nonzero we expect the bubble to shift and deform. The new location and shape can be described by an expansion in terms of angular

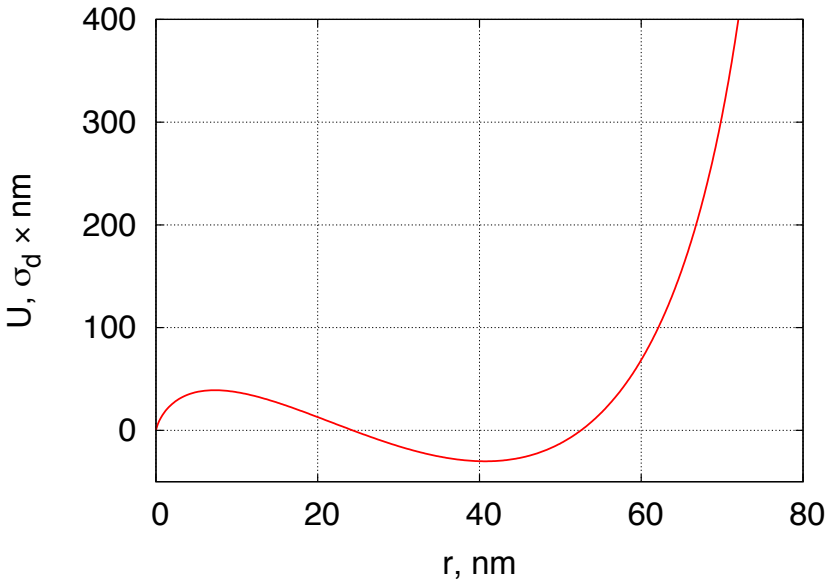

Figure 2.4: Total potential energy U of static bubble as function of average radius.

harmonics:

$$r(\phi) = \overline{r} + \sum_{m=-\infty}^{\infty} \rho_m e^{im\phi} \tag{2.59}$$

Because r is a real variable, $\rho_{-m} = \rho_m^*$. To linear order, the zeroth harmonic ρ_0 describes a change of the average radius $\overline{r}$, the first harmonics $\rho_{\pm 1}$ determine the center of mass $\mathbf{r}_c$, the second harmonics $\rho_{\pm 2}$ describe the ellipticity, and so on.

To make further progress, we need to express the energy of the system in terms of these collective coordinates: $U = U(\rho_m)$. While there is an infinite number of harmonics, only the first few are important in the limit of a weak perturbation g. The form of the possible terms in the energy $U(\rho_m)$ is strongly restricted by the symmetry properties of the harmonics. Under a rotation through an angle ϕ, the

amplitude of the m^{th} harmonic is multiplied by $e^{im\phi}$. At the same time, the energy terms must be invariant. An exception to this rule is the Zeeman energy: a nonzero gradient violates the rotational symmetry. Leaving it out for the moment, we can write, to the lowest order in the harmonics,

$$U_{\text{local}} + U_{\text{stray}} = \text{const} + \sum_{m=-\infty}^{\infty} k_m |\rho_m|^2 + ..., \tag{2.60}$$

where the constant denotes the energy of the circular wall of radius $\overline{r}$ and the omitted terms are of higher orders in $U(\rho_m)$. The Zeeman term evaluates to

$$U_{\text{Zeeman}} = 2\mu_0 M t \pi \overline{r}^2 (g_1 \rho_{-1} + g_{-1} \rho_1) + \dots \tag{2.61}$$

where $g_{\pm 1} = g_x \pm i g_y$. The omitted terms are at least of the third order in ρ_m. At this, quadratic level of approximation, all of the harmonics are decoupled from each other. Minimization of the energy shows that the response to the gradient is limited to the first harmonics:

$$\rho_{\pm 1} = \frac{\mu_0 M t \overline{r}^2}{k_1} g_{\pm 1}, \tag{2.62}$$

while all the other harmonics remain zero.

2.3.4.2 Skyrmion Bubble Dynamics

Our work first deal with description of dynamics of a magnetic bubble: a circular domain wall in a thin ferromagnetic disk with magnetization pointing out of the

disk plane. We aim to examine the dynamics of a bubble in a nonuniform external magnetic field. We have obtained the energetics of magnetic bubble in equilibrium state. Motivated by recent numerical work on this problem [4], we investigate the motion of this magnetic bubble in applied magnetic field. In the absence of the field gradient g, the wall is circular and concentric with the disk. When the field gradient g is nonzero we expect the bubble to shift and deform. The new location and shape can be described by an expansion in terms of angular harmonics:

$$r(\phi) = \overline{r} + \sum_{m=0}^{\infty} a_m \cos m\phi + b_m \sin m\phi \tag{2.63}$$

Each term in this Fourier decomposition Eq. (2.63) has entirely equivalent interpretation as that in Eq. (2.59).

We have obtained the energetics of magnetic bubble in equilibrium state. However, the dynamics of circular domain wall is trickier to analyze as we have to compute various contributions to energy dispersion which involve integral expressions made complicated by circular geometry. In treating Skyrmion magnetic bubble, we have to take into account all the modes in the Fourier decompositions Eqs. (2.59) and (2.63) on equal footing. In writing the Fourier decomposition for $\mathbf{r}$, a vector which points along radial direction away from the origin, all the Fourier modes then point along the same radial direction specified by the angle ϕ. But if we treat the zeroth mode $\overline{r}$ as sort of the dominant mode in terms of magnitude, then we can pursue the same approach as used for straight domain wall by performing expansion in terms

of $\sum_{m=-\infty}^{\infty} \rho_m e^{im\phi}/\overline{r} \equiv \sum_{m=0}^{\infty} \left(a_m \cos m\phi + b_m \sin m\phi\right)/\overline{r}$. The local energy E_{local} (different from the previous discussion on static case, we here have chosen to use E rather than U to denote energy) can be written as,

$$E_{\text{local}} = \sigma \int_w dr = \sigma \int_w |d\mathbf{r}| = \sigma \int_0^{2\pi} |dr(\phi)\hat{\mathbf{e}}_r + r\hat{\mathbf{e}}_\phi d\phi|$$

with $\sigma = 4At/\xi$ and

$$\mathbf{r} = r\hat{\mathbf{e}}_r,\ d\mathbf{r} = dr\hat{\mathbf{e}}_r + r\hat{\mathbf{e}}_\phi d\phi \tag{2.64}$$

$$r = \overline{r} + \sum_{m=0}^{\infty} a_m \cos m\phi + b_m \sin m\phi,\ dr = \sum_{m=0}^{\infty} (-a_m m \sin m\phi + m b_m \cos m\phi) d\phi \tag{2.65}$$

Eq. (2.65) indicates that we use a polar coordinate system with average radius $\overline{r}$ as the reference coordinate system for arbitrarily deforming circular domain wall that we have. The vector position of a point on the wall is decomposed into its projections in radial and tangential directions of the polar coordinate, at a given polar angle ϕ. Using these, the local energy becomes

$$E_{\text{local}} = \sigma \int_0^{2\pi} d\phi \sqrt{r^2 + \left(\frac{dr}{d\phi}\right)^2} = \sigma\overline{r} \int_0^{2\pi} d\phi \sqrt{1+x} \tag{2.66}$$

with

$$x = \frac{(\frac{dr(\phi)}{d\phi})^2 + 2\overline{r}(r(\phi) - \overline{r}) + (r(\phi) - \overline{r})^2}{\overline{r}^2}$$

We perform Taylor series expansion of the terms inside square bracket $\sqrt{1+x} = 1 + \frac{1}{2}x - \frac{1}{8}x^2 + O(x^3)$. Retaining only up to second order terms in a_m, b_m, we have

$$E_{\text{local}} = 2\pi\sigma(\overline{r} + \rho_0) + \sum_{m=-\infty}^{\infty} |\rho_m|^2 \epsilon_m^{\text{local}} = 2\pi\sigma(\overline{r} + \rho_0) + \frac{1}{2}\sum_{m=0}^{\infty}(a_m^2 + b_m^2)\epsilon_m^{\text{local}} \quad (2.67)$$

where $\epsilon_m^{\text{local}} = \frac{\pi\sigma}{\overline{r}} m^2$. This term is nothing but the analog to vibrating string elastic potential energy to be considered later when deriving the wave spectrum so that it will not need be introduced by hand. For the wall-wall dipolar energy,$E_{\text{wall-wall}}$, we have first the 'static energy' part computed before, previously referred to as U_{stray1},

$$U_{\text{stray1}} = -2\overline{r}[\ln(4\overline{r}/a) - 2] \quad (2.68)$$

where $a = (t/2)\exp(-3/2)$.

The dynamical $E_{\text{wall-wall}}$ is obtained by evaluating

$$E_{\text{wall-wall}} = -\frac{\Omega}{2\pi}\int \frac{d\mathbf{r}.d\mathbf{r}'}{|\mathbf{r} - \mathbf{r}'|} \quad (2.69)$$

where $\Omega = \mu_0 M^2 t^2$ as stated before. The calculation of this expression is similar to that for E_{local} but now we have to write $\mathbf{r}$ and $\mathbf{r}'$ in terms of their Fourier modes as in Eq. (2.64) or Eq. (2.65). The geometry can be based on Fig. 2.5.

The calculation of $E_{\text{wall-wall}}$ is tedious but straightforward and gives the net correction to wall-wall energy can therefore be written as

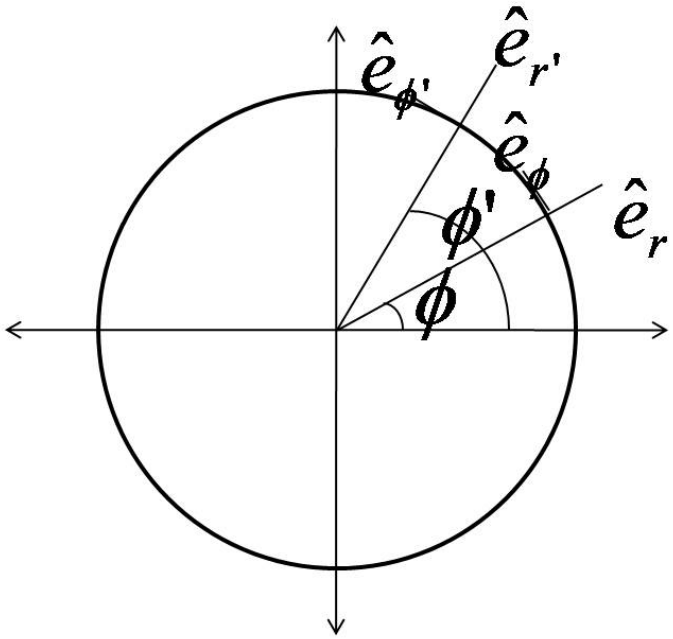

Figure 2.5: Polar coordinate system used to compute bubble energy.

$$E^{r}_{\text{wall}-\text{wall}} = \sum_{m=0}^{\infty} (a_m^2 + b_m^2)\epsilon_m^{(w-w)} \tag{2.70}$$

where

$$\epsilon_m^{(w-w)} = -\frac{\Omega}{8\overline{r}}(I_m + J_m + K_m + L_m) \tag{2.71}$$

where

$$I_m = \int_{-\pi+\Delta\phi}^{\pi-\Delta\phi} d\phi \frac{(1+m)^2\cos(2m+2)\phi + (1-m)^2\cos(2m-2)\phi}{|\sin\phi|}$$

$$J_m = \frac{3}{2}\int_{-\pi+\Delta\phi}^{\pi-\Delta\phi} d\phi \frac{\cos 2\phi(1+\cos 2m\phi)}{|\sin\phi|}$$

$$K_m = -\int_{-\pi+\Delta\phi}^{\pi-\Delta\phi} d\phi \frac{(1+m)\cos\left((2m+2)\phi\right)+(1-m)\cos((2m-2)\phi)+2\cos 2\phi}{|\sin\phi|}$$

$$L_m = \frac{1}{2}\int_{-\pi+\Delta\phi}^{\pi-\Delta\phi} d\phi \frac{\cos(2\phi)(-1+\cos(2\phi)\cos(2m\phi))}{|\sin\phi|^3}$$

For the wall-edge dipolar energy, the 'static' part has been computed before as the U_{stray2}

$$U_{\text{stray2}} = 4\Omega R\overline{r}\int_0^{\pi/2} d\phi \frac{1-2\sin^2\phi}{\sqrt{(R-\overline{r})^2+4R\overline{r}\sin^2\phi}} = 2\Omega(R+\overline{r})\left(\frac{R^2+\overline{r}^2}{(R+\overline{r})^2}K(k)-E(k)\right) \tag{2.72}$$

To get the dynamical correction to this static energy, here to be referred to as $E_{\text{wall-edge}}$, we perform the same expansion in terms of similar small expansion parameter as we used for $E_{\text{wall-wall}}$, where now $\frac{1}{|\mathbf{r}-\mathbf{R}|} \equiv (1+x)^{-1/2} = 1-\frac{1}{2}x+\frac{3}{8}x^2+O(x^3)$.

$$E_{\text{wall-edge}} = \frac{\Omega}{2\pi}\int \frac{d\mathbf{r}.d\mathbf{R}}{|\mathbf{r}-\mathbf{R}|}$$

Once again, the calculation of this expression is delicate but straightforward and gives for the net correction to equilibrium $E_{\text{wall-edge}}$,

$$E_{\text{wall-edge}} = \sum_{m=0}^{\infty}(a_m^2+b_m^2)\epsilon_m^{(w-e)} \tag{2.73}$$

where

$$\epsilon_m^{(\mathrm{w-e})} = f(R,\overline{r}) + g(R,\overline{r}) + h(R,\overline{r}) + k(R,\overline{r}) \tag{2.74}$$

and

$$f(R,\overline{r}) = 2\Omega R^2 \int_0^{\pi/2} d\phi \frac{\cos^2 2\phi}{\left((R-\overline{r})^2 + 4R\overline{r}\sin^2\phi\right)^{3/2}}$$

$$g(R,\overline{r}) = -2\Omega R\overline{r} \int_0^{\pi/2} d\phi \frac{\cos 2\phi}{\left((R-\overline{r})^2 + 4R\overline{r}\sin^2\phi\right)^{3/2}}$$

$$h(R,\overline{r}) = -\Omega R\overline{r} \int_0^{\pi/2} d\phi \frac{\cos 2\phi}{\left((R-\overline{r})^2 + 4R\overline{r}\sin^2\phi\right)^{3/2}}$$

$$k(R,\overline{r}) = 3\Omega R\overline{r} \int_0^{\pi/2} d\phi \frac{\cos 2\phi\,(\overline{r} - R\cos 2\phi)^2}{\left((R-\overline{r})^2 + 4R\overline{r}\sin^2\phi\right)^{5/2}}$$

The total energy of bubble in this dynamic case is given by, to quadratic order in a_m, b_m

$$E = E_{\mathrm{local}} + E_{\mathrm{wall-wall}} + E_{\mathrm{wall-edge}}$$

$$= 2\pi\sigma(\overline{r}+\rho_0) - 2\overline{r}[\ln(4\overline{r}/a) - 2] + 2\Omega(R+\overline{r})\left(\frac{R^2+\overline{r}^2}{(R+\overline{r})^2}K(k) - E(k)\right) + \sum_{m=-\infty}^{\infty} |\rho_m|^2 \epsilon_m \tag{2.75}$$

where

$$\epsilon_m = \frac{\pi\sigma m^2}{\overline{r}} - \frac{\Omega}{4\overline{r}}\Sigma_{\text{wall}-\text{wall}} + 2\Sigma_{\text{wall}-\text{edge}} \tag{2.76}$$

with

$$\Sigma_{\text{wall}-\text{wall}} = I_m(\overline{r}) + J_m(\overline{r}) + K_m(\overline{r}) + L_m(\overline{r})$$

$$\Sigma_{\text{wall}-\text{edge}} = f(R,\overline{r}) + g(R,\overline{r}) + h(R,\overline{r}) + k(R,\overline{r})$$

where the terms on the right hand sides are as given following Eqs. (2.71) and (2.74). We observe that the total energy E as well as the mode energy ϵ_m is function of average radius $\overline{r}$.

Now we allow magnetization vector field on the circular domain wall to deviate from being tangential to the wall. We define the coordinate system for such dynamics as illustrated in Fig. 2.6.

We assume harmonic potential for energy cost of having nonzero deviation of magnetization vector field from the tangent to the wall; $V[\frac{1}{\overline{r}}\frac{\partial r}{\partial\phi} - \psi] = \int ds \frac{\sigma_\phi}{2}\left(\frac{1}{\overline{r}}\frac{\partial r}{\partial\phi} - \psi\right)^2$ where $ds = \sqrt{(dr)^2 + (rd\phi)^2}$. The elastic energy analog of massive vibrating string will be assumed $V[\frac{1}{\overline{r}}\frac{\partial r}{\partial\phi}] = \int ds \frac{\sigma_s}{2}(\frac{\partial r}{\overline{r}\partial\phi})^2$, but this is already included in local energy E_{local} so that we do not have to put it in by hand. Note that we have assumed a small deformation of circular domain wall for the form of $V[\frac{1}{\overline{r}}\frac{\partial r}{\partial\phi} - \psi]$ and $V[\frac{1}{\overline{r}}\frac{\partial r}{\partial\phi}]$ used here to be valid, particularly because the gradient $\frac{\partial r}{\partial s} \approx \frac{1}{\overline{r}}\frac{\partial r}{\partial\phi}$ is valid only for small deformation δr in $r = \overline{r} + \delta r$. For the kinetic energy term, we assume Berry's phase

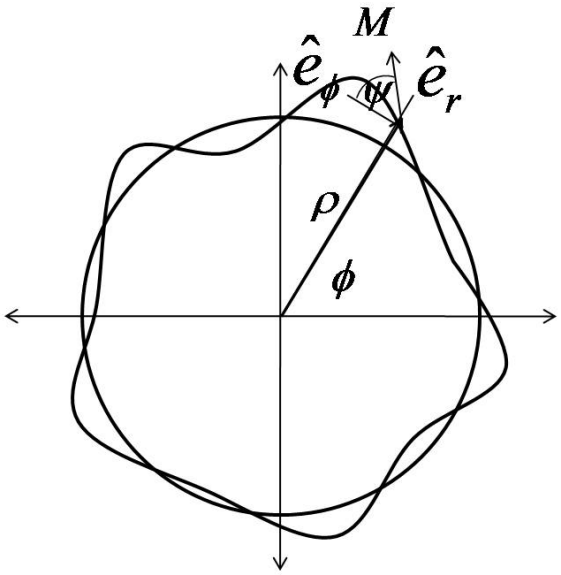

Figure 2.6: Coordinate system for dynamical magnetic bubble with two dynamical variables ρ and ψ.

kinetic term of the form $\int dsg\dot{r}\psi = 2\pi\overline{r}g\dot{r}\psi$. The full Lagrangian in Fourier space takes the form;

$$L = \sum_{m=-\infty}^{\infty} \left[-i\omega 2\pi\overline{r}g\rho_m\psi_m^* - \epsilon_m \left|\rho_m\right|^2 - \pi\kappa\overline{r}\left|\frac{im\rho_m}{\overline{r}} - \psi_m\right|^2 \right] \tag{2.77}$$

where ϵ_m is given by Eq. (2.76). Here we use for this Skyrmion magnetic bubble the the same coefficients $\sigma_\phi = \kappa$ and $\sigma_s = \sigma$ as those used for straight domain wall case. The corresponding equations of motion in Fourier space obtained by taking $\partial L/\partial\rho_m = \partial L/\partial\psi_m = 0$ are given by

$$\begin{aligned} i\left(2\pi\overline{r}\omega g - 2\pi m\kappa\right)\psi_m + \left(2\epsilon_m + \frac{2\pi\kappa m^2}{\overline{r}}\right)\rho_m = 0 \\ -i\left(2\pi\overline{r}\omega g - 2\pi m\kappa\right)\rho_m + 2\pi\overline{r}\kappa\psi_m = 0 \end{aligned} \tag{2.78}$$

which give rise to wave spectrum

$$\omega = \frac{m\kappa}{\bar{r}g} \pm \frac{1}{2\pi\bar{r}g}\sqrt{\kappa\left(4\pi^2\kappa m^2 + 4\pi^2\sigma m^2 - \pi\Omega\Sigma_{\text{wall}-\text{wall}}\right) + 8\kappa\pi\bar{r}\Sigma_{\text{wall}-\text{edge}}} \tag{2.79}$$

The $\pm$ sign correspond to counter clockwise and clockwise propagating waves, respectively. Eq. (2.76) is the 'true bubble' version of the wave spectrum of straight domain wall in a strip Eq. (2.18). The profile of the spectrum of the two waves is given in Fig. 2.7.

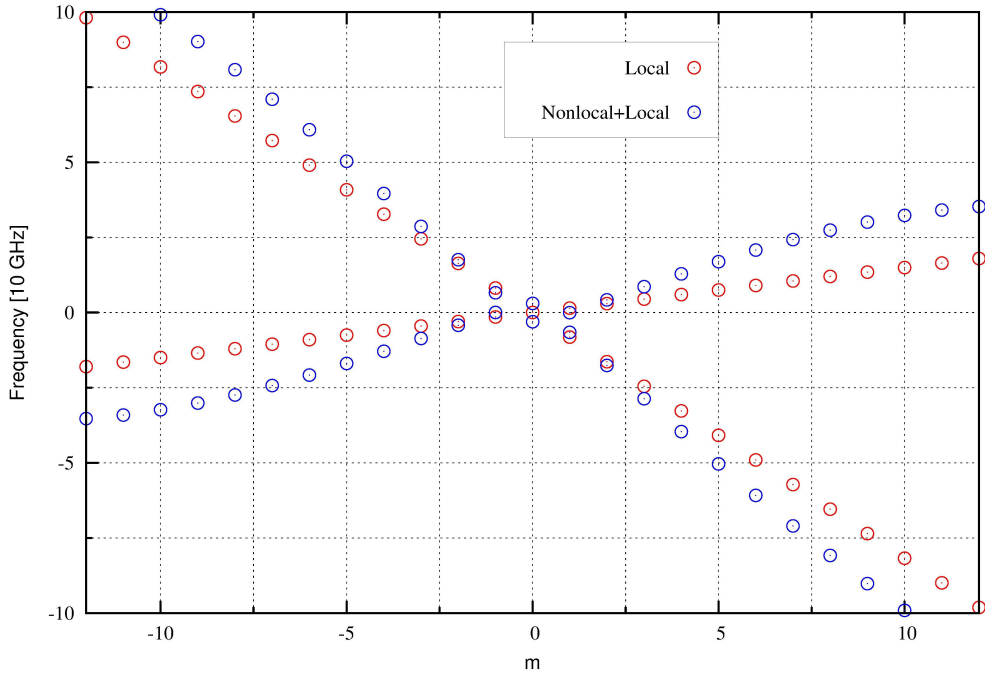

Figure 2.7: Wave spectrum of circular domain wall with dipolar interaction.

We see the nontrivial feature at $m = 0$ which is an effect of long range dipolar interaction. The full spectrum however suffers from an oscillatory behavior which is an artifact of the cutoff, given that we have chosen cutoff $a = 0.5t\,\exp(-3/2)$.

However, Fig. 2.7 shows that in the range of mode index ($1 < m < 11$) which has been chosen to be such that a direct comparison with straight domain wall case is valid, which is in the short distance (but still larger than short distance cutoff) or large wave vector limit, the wave spectrum of theory that includes long range dipolar interaction asymptotically comes close enough to the spectrum with only local energy terms. The deviation between the two at $m \sim 11$ is however the effect of the artifact oscillatory behavior, compared to the straight domain wall case where the two asymptotically approach each other at larger k. With this observation, care must be taken to estimate the asymptotic value of the speeds of the wave with dipolar interaction, but as a reference, without such interaction, from Eq. (2.79), the ratio of the two speeds is

$$\left.\frac{c_{ccw}}{c_{cw}}\right|_{\text{local}} = \left.\frac{\omega_+}{\omega_-}\right|_{\text{local}} = \frac{\kappa + \sqrt{\kappa(\kappa+\sigma)}}{\kappa - \sqrt{\kappa(\kappa+\sigma)}} = -5.59$$

as compared to numerical simulation result which predicts $c_{ccw}/c_{cw} \simeq -5.29$. The small discrepancy suggests for more accurate modeling of the Skyrmion bubble domain wall.

We have therefore completed the calculations for dynamical Skyrmion magnetic bubble where we have obtained the energy dispersion for low energy modes and used that to analyze the dynamics of Skyrmion magnetic bubble by deriving the equations of motion and the associated wave spectrum. We will describe in the following section, our numerical simulation from which we get numerical result on the wave spectrum

which we compare with the analytical result obtained above.

2.4 Numerical Simulation

We have performed numerical simulations to measure the frequency spectrum of waves with higher azimuthal numbers m. We used the same geometry and material parameters as Moutafis *et al.* [4]: a FePt disk of radius $R = 80$ nm, thickness $t = 32$ nm, magnetization $M = 10^6$ A/m, exchange constant $A = 10^{11}$J/m, easy-axis anisotropy $K = 1.3 \times 10^6 \mathrm{J/m^3}$, and gyromagnetic ratio $\gamma = 1.75 \times 10^{11}$ sA/kg. These give the quality factor $Q = 2.06$ and exchange length $\lambda = 4.0$ nm. We utilized micromagnetic simulator OOMMF [53] in the two-dimensional regime with a unit cell of 1.25 nm. The equilibrium radius of the bubble was $\overline{r} = 37$ nm. The free motion of the m^{th} harmonic of $\rho(\phi)$ was fitted by a sum of two underdamped components. The extracted frequencies are shown in Fig. 2. The theoretical curve is the straight-wall spectrum (16) with $k = m/\overline{r}$. We used the mass density extracted from the simulation of the $m = 1$ mode, $\rho = \mathcal{M}_{sim}/\pi\overline{r}$, and set the effective width w equal to the disk radius. The theory works quite well for the slow mode, less so for the fast one.

We repeat the numerical simulations first performed by Moutafis *et al.* [4] to extract the lowest mode frequencies from which we determine the important parameters of the theory. We first determine the location of the wall. This is crucial in view of one of the most important ideas discovered in this study that the dynamics of the wall

is determined not mainly by the motion of the center of mass of the Skyrmion bubble, located inside the bubble where magnetization is practically uniform and nothing quite interesting happens, but rather, by the motion of the domain wall itself, where the nontrivial dynamics involving but the wall and the magnetization vector giving rise to transverse modes occurs.

We define the domain wall as a line of points in the plane of the film where out-of-plane magnetization $M_z(x, y)$ vanishes. Because our numerical simulations were done on a discrete lattice, we needed an algorithm to extract a continuous line from discrete data points. The location of the domain wall was determined in two steps: we first identified a discrete set of points with $M_z = 0$; we then fit their positions to a line, Eq. (2.5).

The first step is illustrated in Fig. 2. The magnetization at the boundary of a cell is determined by interpolation with the magnetization at the center of the current cell and its nearest neighbors as follows:

$$\mathbf{M}_{i,j+\frac{1}{2}} = (\mathbf{M}_{i,j} + \mathbf{M}_{i,j+1})/2,$$

$$\mathbf{M}_{i+\frac{1}{2},j} = (\mathbf{M}_{i,j} + \mathbf{M}_{i+1,j})/2,$$

$$\mathbf{M}_{i+\frac{1}{2},j+\frac{1}{2}} = (\mathbf{M}_{i,j} + \mathbf{M}_{i,j+1} + \mathbf{M}_{i+1,j} + \mathbf{M}_{i+1,j+1})/4.$$

If the wall intersects the cell then the sign of M_z at one or more points at its boundary differs from that at the center of the cell. At the crudest level, we could use the centers of intersected cells as a proxy for the location of the domain wall. To refine

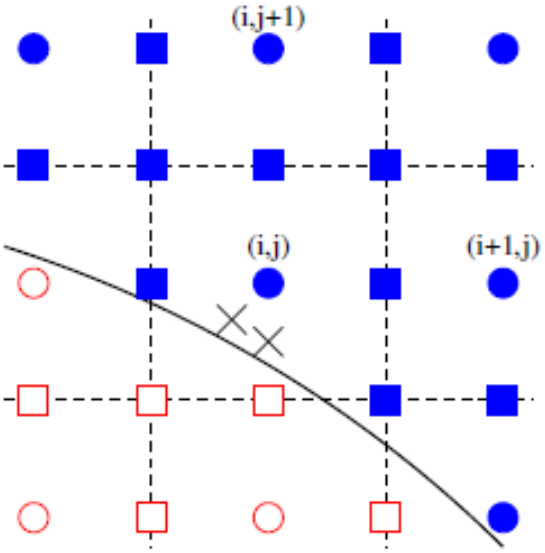

Figure 2.8: Tracing a domain wall.

The domain wall is represented by solid line. Circles denote the centers of lattice cells in the simulation. Squares are points at cell boundaries (dashed lines). Crosses are locations of the domain wall obtained by linear extrapolation. Open red symbols mean $M_z > 0$, filled blue symbols mean $M_z < 0$.

this result, we used a linear interpolation for M_z between the center of a cell and the points on its boundary to find the locations with $M_z = 0$. The refinement reduced the discretization noise by a factor of 70, which was particularly important for modes with higher azimuthal numbers, which had small amplitudes.

We also consider the motion of the center of mass of the Skyrmion bubble by reproducing the simulations of Moutafis *et al.* [4] in order to fit the numerical results with phenomenological expression for lowest mode frequencies in Eq. (2.4) which give the motion of the center of the Skyrmion bubble. The motion of the center of mass (X, Y) of a magnetic bubble is conveniently represented by a complex variable $r_1 = (X - iY)/2$. The general motion of a bubble with inertial mass $\mathcal{M}$ and a gyrotropic coefficient $\mathcal{G}$ in a parabolic potential with stiffness $\mathcal{K}$ is a superposition of two spiral motions:

$$r_1(t) = \sum_{m=\pm 1} a_m e^{i\omega_m t - \Gamma_m t}. \tag{2.80}$$

For weak dissipation, $\Gamma_m \ll \omega_m$

$$\omega_{\pm 1} \approx -\frac{\mathcal{G}}{2\mathcal{M}} \pm \sqrt{\left(\frac{\mathcal{G}}{2\mathcal{M}}\right)^2 + \frac{\mathcal{K}}{\mathcal{M}}}, \; \frac{\Gamma_{+1}}{\Gamma_{-1}} \approx \left|\frac{\omega_{+1}}{\omega_{-1}}\right|. \tag{2.81}$$

The top panel of Fig. 1 shows the best fit to Eq. (2.80) with $\omega_{+1}/2\pi = 0.97$ GHz, $\Gamma_{+1} = 0.25$ ns^{-1}, $\omega_{-1}/2\pi = -4.27$ GHz, and $\Gamma_{-1} = 1.0$ ns^{-1}. A small systematic deviation between the best-fit line and the data is plotted in the bottom panel of Fig. 1. Much of it can be accounted for by a superposition of two spiral motions with

frequencies $\omega_{+1} \pm \omega_0$, where $\omega_0/2\pi = 3.15$ GHz is the eigenfrequency of the bubble's breathing mode. This is likely the effect of an anharmonic coupling between the two modes.

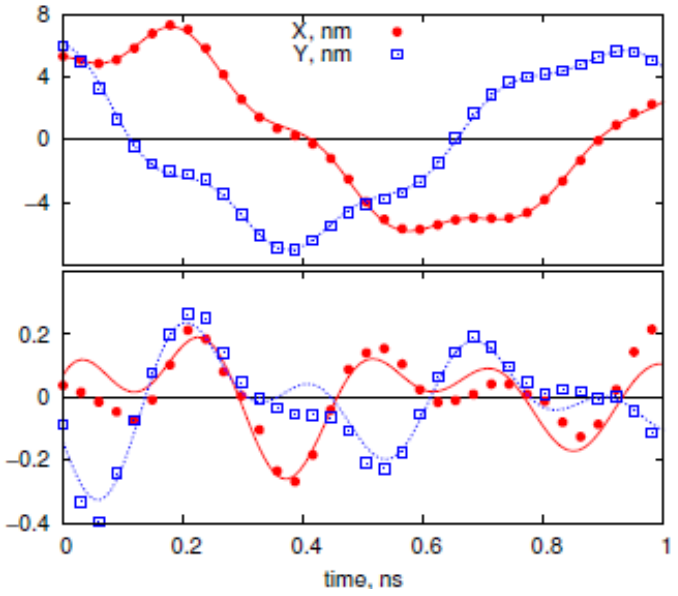

Figure 2.9: The numerical simulated motion of center of mass of Skyrmion bubble. Top panel: The displacement of the bubble's center of mass (X, Y) as a function of time (points) and the best fit to the two-mode approximation (A1) (lines). Bottom panel: The difference between the data and the best fit (points) and the best fit to a superposition of two spiral motions with frequencies $\omega_{+1} \pm \omega_0$ (lines). The vertical scales in the two panels differ by a factor of 30.

We thus conclude that any unidentified modes contribute no more than 0.1 nm in amplitude, or about 1 per cent, to the center-of-mass motion. This completes the description of our numerical simulation of Skyrmion bubble dynamics.

2.5 Conclusion

The widely used Thiele's equation (2.2) predicts that magnetic textures with a Skyrmion number $q \neq 0$ behave as massless particles moving in a uniform magnetic field and an external potential. Although this approach works very well for magnetic vortices ($q = \pm 1/2$), it fails for Skyrmion magnetic bubbles ($q = \pm 1$). Here we have shown that a Skyrmion bubble behaves as a massive object and have explained the origin of its mass. A Skyrmion bubble possesses additional modes, which are best viewed as transverse fluctuations of its edge. These waves are chiral; i.e., they propagate with different speeds in opposite directions. The nonreciprocal wave propagation is expected in other geometries, e.g., striped and labyrinthine domains.

We see that we have found a new type of dynamics where the standard phenomenological approach in the form of Thiele equation which has been so successful in describing most topological defects in ferromagnet does not work in this case. The important message we conclude in this finding is that for topological defect where gyrotropic coupling between the domain wall and transverse mode is important in the dynamics, such as in the Skyrmion bubble that we study, this mass inertia term is important. What happened with the older studies is that this gyrotropic coupling to the transverse mode is negligible, the stiffness κ is so large and thus the magnetization vector is strongly fixed to be tangential to the wall so that the transverse modes are not active in practice. This makes Thiele's phenomenological description works so well, such as that for vortex. The result also emphasizes the importance of

gyrotropic coupling in the dynamics of Skyrmion bubble and this gyrotropic coupling itself is the source of the mass (inertia) of the bubble. This is to be compared with other studied topological defects where either conservative force or damping force is the dominant effect and so the mass or inertia effect does not show up.

In a Skyrmion crystal, the discrete modes of a bubble turn into excitation branches. The slow and fast $m = 1$ modes give rise to the magnetophonon and cyclotron branches [54]; the cyclotron frequency $\omega = \mathcal{G}/\mathcal{M}$ is in the GHz range. The $m = 0$ breathing mode has been seen in numerical simulations [55]. The breathing mode and one of the $m = 1$ modes have been found in Cu_2OSeO_3 [56]. Branches with higher m may also be detectable.

We have not studied processes where topological charge changes due to application of strong magnetic field pulse, as has been studied numerically by Moutafis *et al.* [4] where the topological charge switches between 1 and 0. The resulting dynamics is even more nontrivial but we believe that an extension of our result to this more complicated case is feasible.

Technically, we also learn a lesson that we have to be careful in dealing with problematic long range interaction such as dipolar interaction which has unfavorable behavior both in long distance and short distance limits. This is actually quite expected and quite reminiscent of the problem of divergence of self energy of electron in classical and quantum electrodynamics that frustrated theorists in the early days of the birth of quantum field theory.

Chapter 3

Quantum Phase Transition in Pyrochlore Quantum Spin Ice

This chapter discusses novel phenomenon that we find to occur in the quantum criticality of pyrochlore quantum spin ice. To be precise, we predict the occurrence of fluctuation-induced first order quantum phase transition between $U(1)$ quantum spin liquid and antiferromagnet phases of pyrochlore quantum spin ice. The chapter begins with a general introduction to the subject in Section 3.1. We proceed with a description of a model of pyrochlore quantum spin ice in Section 3.2. The effective low energy description is derived in Section 3.3. The free energy description and mechanism of the fluctuation-driven critical phenomenon and its main properties are elucidated in Section 3.4. The chapter ends with concluding discussion 3.5. Part of the results presented in this chapter has been submitted as arXiv:1307.5804 [57].

3.1 Introduction

Quantum spin liquid (QSL), the exotic state with no magnetic order down to very low temperatures has been the subject of intensive studies since its very first suggestion by P.W. Anderson on the existence of resonating valence bond type of such state in triangular lattice [5] and the idea that QSL may be the physics behind high T_c cuprates [58]. The search for quantum spin liquid state has expanded to other systems especially in frustrated quantum magnets [7] where geometric and quantum fluctuations work together to prevent magnetic ordering and deliver quantum spin disordered states; the QSL. In spin systems, theoretical studies suggest the existence of phase with Coulomb type power law correlations, hence called Coulomb phase [20] [21] and of $U(1)$ quantum spin liquid which is described by emergent quantum electrodynamics with emergent photons (gauge field) in the quantum regime. Such $U(1)$ QSL has been argued to exist in pyrochlore lattice, a 3-d frustrated lattice spins, in the easy axis limit [21].

Pyrochlore lattice (Fig. 3.1) has been found in several magnetic oxide compounds with rare-earth elements. As noted in the Introduction Chapter, earlier-discovered pyrochlore compounds especially those from the families of $Dy_2Ti_2O_7$ and $Ho_2Ti_2O_7$ constitute magnetic systems with predominantly classical dipolar interactions, whereas more recent families of pyrochlore compounds such as $Pr_2Sn_2O_7$, $Er_2Ti_2O_7$, and $Yb_2Ti_2O_7$ are characterized by dominant short range quantum spin exchange interaction [15]. We will focus on this latter system. We will be interested more in the

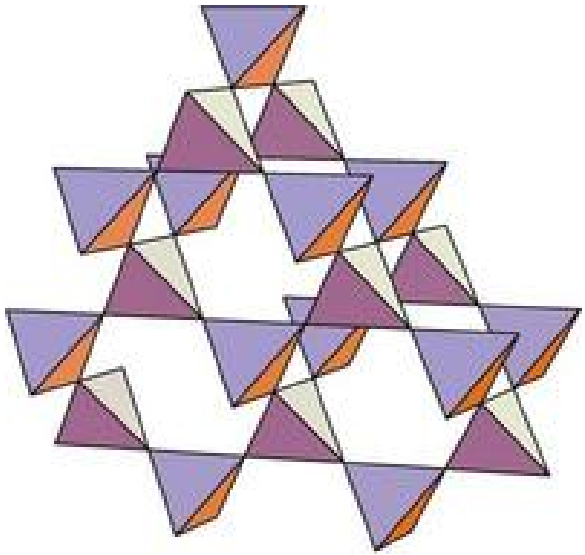

Figure 3.1: Pyrochlore lattice with up and down tetrahedra [59].

effective low energy description of the system appropriate (and sufficient) to describe the physics in the vicinity of quantum critical regime, rather than the full energy range and microscopic description that is needed to get more complete picture of the physics, such as the full phase diagram, which can be obtained from mean field theory as has been performed in several recent studies on this subject.

We will use a minimal pseudospin-1/2 model to describe the low-energy physics of magnetic pyrochlore oxides associated with local magnetic doublets of rare-earth ions. This model was first introduced on symmetry grounds [22]. It has also been derived microscopically using superexchange theory for various materials [23] [60] [61]. The pseudospin originates from the atomic Kramers ground doublet of the LS coupling and the crystalline electric field, which is almost described with $J^z = \pm 1/2$. The model Hamiltonian was calculated microscopically as the sum of Anderson's superexchange

interaction and the magnetic dipole interaction and was found to show a strong exchange anisotropy [23]. The model has been used to explain the structure factor and the spectrum of spin waves experimentally observed in $Yb_2Ti_2O_7$ [22] [62]. In this model, the putative continuous rotational symmetry of the pseudospins is broken by a significant level of magnetic anisotropy. Moreover, at least for some materials, the Ising interaction coupling J_{zz} normally remains the strongest exchange coupling which will give rise to quantum spin ice physics [63]. For the actively studied $Yb_2Ti_2O_7$ however, K. A. Ross *et al.* found $J_{zz} = 0.17 \pm 0.04$ meV, $J_{\pm} = 0.05 \pm 0.01$ meV, $J_{\pm\pm} = 0.05 \pm 0.01$ meV, and $J_{z\pm} = -0.14 \pm 0.01$ meV [22] suggesting that the transverse $J_{z\pm}$ coupling can possibly compete with the Ising coupling J_{zz}. Recent experimental findings suggest the relevance of the Coulomb phase physics [20] in real rare-earth magnetic pyrochlore oxides [22] [62] at least at a phenomenological level.

Savary and Balents [24] developed a novel method to analyze this problem based on a gauge theory reformulation of the problem on a dual diamond lattice. They re-expressed the original Hamiltonian as a problem of bosonic spinons hopping in the background of a fluctuating compact $U(1)$ gauge field followed by mean-field approximation. Bosonic spinon in this case is spin-carrying elementary excitation with bosonic quantum statistic. In their work, this gauge mean-field theory (gMFT) was applied to the regime of the phase diagram approximately appropriate to $Yb_2Ti_2O_7$, with $J_{\pm\pm} = 0$, and $J_{\pm} > 0$. They found $U(1)$ QSL phase and an additional exotic state, a Coulomb ferromagnet within a narrow domain of stability in the phase dia-

gram. We will consider the same Hamiltonian as Ref. [24] to probe the regime near quantum criticality but use full gauge theory formulation rather than gauge mean field theory.

Quantum phase transition (QPT) [11] [12] [13] between these phases is fascinating problem because of the possibility for non-Ginzburg-Landau type of conventional phase transition [65]. Ginzburg-Landau theory of phase transition models transition between ordered state and disordered state described by an order parameter in terms of free energy which at lowest order takes the form of ϕ^4 field theory. This will give rise to second order phase transition (according to Ehrenfest's classification) where the order parameter changes continuously across the critical point. This turns out to be very good description of many classical phase transitions such as that in ferromagnet [66] [67]. In the past few decades, researchers have discovered several new types of phase transition that require novel description beyond that of Ginzburg-Landau. There are phase transitions that cannot be described by symmetry breaking or in terms of order parameter and are topological in character, such as Berezinskii-Kosterlitz-Thouless (BKT) transition [68] [69]. There are also phase transitions that defy Ginzburg-Landau prediction such as the so-called deconfined QPT which is transition between two phases with different order parameters that is supposed to be first order based on Ginzburg-Landau theory but turns out to be second order [70]. The change in order is associated with emergent gauge field and deconfined fractional excitations. At finite temperatures [71] [72] or at low temperatures near quantum

criticality [73] [74] [75], in systems which involve coupling of order parameter to soft modes, such as electromagnetic field or coupling of one order parameter to the phase fluctuations of competing order, a second order phase transition can be driven to first order one by the gauge fluctuations. We will show in this work that similar effect but at $T = 0$ occurs between QSL and its neighboring antiferromagnetic (AFM) phase in pyrochlore quantum spin ice due to quantum fluctuations and coupling of order parameter to gauge field. Similar phenomenon in different context; clean itinerant ferromagnet, was discussed using renormalization group approach [76]. A general study of stability of quantum critical point that involves coupling to competing order parameter found that the QPT can be driven from second order to first order, as discussed by [77]. Different from these previous studies, we will show that fluctuation-induced first order quantum phase transition occurs in system with emergent $U(1)$ gauge theory (quantum electrodynamics) as is the case in pyrochlore quantum spin ice.

3.2 Model of Pyrochlore Quantum Spin Ice

We consider microscopic model of pyrochlore quantum spin ice in the form of the most general symmetry-allowed Hamiltonian with bilinear spin interaction [22] [23]. With the spin defined on pyrochlore lattice site and considering only nearest-neighbor

exchange coupling sufficient for strongly localized f-electron states, the Hamiltonian and neglecting dipole interaction, written in global spin coordinates is given by

$$H = \frac{1}{2}\sum_{ij} J_{ij}^{\alpha\beta} S_i^{\alpha} S_j^{\beta} \tag{3.1}$$

where $J_{ij}^{\alpha\beta} = J_{ji}^{\beta\alpha}$ is the matrix of exchange couplings between sites i and j where $i, j = 0, 1, 2, 3$ representing the four sites in a tetrahedron whereas $\alpha, \beta = x, y, z$. Symmetry consideration [64] allows four independent exchange constants, J_1, J_2, J_3, J_4 which can be specified by giving the exchange matrix on one pair of nearest neighbor sites, located at positions $\mathbf{r}_0 = a(1,1,1)/8$ and $\mathbf{r}_1 = a(1,-1,-1)/8$ on a tetrahedron centered at the origin. In this case, a is the conventional cubic lattice spacing for the face centered cubic (FCC) Bravais lattice:

$$\mathbf{J}_{01} = \begin{pmatrix} J_2 & J_4 & J_4 \\ -J_4 & J_1 & J_3 \\ -J_4 & J_3 & J1 \end{pmatrix} \tag{3.2}$$

The other exchange matrices can be obtained from this one by cubic rotations. One can use the usual coordinate system for the pyrochlore lattice, with sites located on tetrahedra whose centers form a FCC lattice. One may consider a tetrahedron to be centered at the origin with its four corners at $\mathbf{r}_0 = a(1,1,1)/8, \mathbf{r}_1 = a(1,-1,-1)/8, \mathbf{r}_2 = a(-1,1,-1)/8, \mathbf{r}_3 = a(-1,-1,1)/8$. The exchange matrices $\mathbf{J}_{ij}$ between sites of types i and j are obtained by applying the following cubic rotations

R_{ij} to $\mathbf{J}_{01}$ [22]:

(i) R_{02} is a $2\pi/3$ rotation about the [111] axis,

(ii) R_{03} is a $4\pi/3$ rotation about the [111] axis,

(iii) R_{21} is a $4\pi/3$ rotation about the $[1\overline{1}\overline{1}]$ axis,

(iv) R_{31} is a $2\pi/3$ rotation about the $[1\overline{1}\overline{1}]$ axis,

(v) R_{23} is a rotation made of a $2\pi/3$ rotation about the [111] axis followed by a $4\pi/3$ rotation about the $[1\overline{1}\overline{1}]$ axis. One can make use of local cubic basis vectors

$$\hat{\mathbf{e}}_0 = (1,1,1)/\sqrt{3}, \quad \hat{\mathbf{e}}_1 = (1,-1,-1)/\sqrt{3},$$
$$\hat{\mathbf{e}}_2 = (-1,1,-1)/\sqrt{3}, \quad \hat{\mathbf{e}}_3 = (-1,-1,1)/\sqrt{3} \tag{3.3}$$

where the vectors point from the center of a tetrahedron towards its four corners, as illustrated in Fig. 3.2.

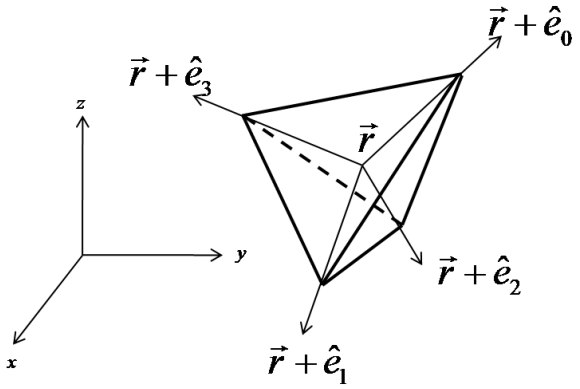

Figure 3.2: A tetrahedron and its four local cubic basis vectors, which are to be used as the local z spin axis in the pyrochlore model that we study.

The five rotation processes mentioned before can then be represented by the fol-

lowing matrix

$$\gamma_{\mu\nu} = \begin{pmatrix} 0 & 1 & w & w^2 \\ 1 & 0 & w^2 & w \\ w & w^2 & 0 & 1 \\ w^2 & w & 1 & 0 \end{pmatrix} \tag{3.4}$$

where $w = \exp(i2\pi/3)$. The four unit vectors $\hat{\mathbf{e}}_\mu$ physically point from the center of a tetrahedron to its four corners. Each defines the local spin z axis of the spin at the corresponding site at the corner. We will however use these four unit vectors as (nonorthogonal) global basis vectors which are directly related to the $\hat{\mathbf{x}}$, $\hat{\mathbf{y}}$, and $\hat{\mathbf{z}}$ unit vectors of global 3-d Cartesian coordinate. Their relation can be written as,

$$\hat{\mathbf{e}}_\mu = \sum_{\alpha=1,2,3} n_{\mu\alpha}\hat{\mathbf{e}}_\alpha \tag{3.5}$$

where the coefficient $n_{\mu\alpha}$ is nothing but the α^{th} element of $\hat{\mathbf{e}}_\mu$. One can then rewrite the zero-field Hamiltonian Eq. (3.1) in terms of spins quantized along the local C_3 axis for each site S_i^μ which acts as local spin operator and using the relations $J_{zz} = -[2J_1 - J_2 + 2(J_3 + 2J_4)]/3, J_\pm = [2J_1 - J_2 - J_3 - 2J_4]/6, J_{\pm\pm} = [J_1 + J_3 - 2J_3 + 2J_4]/6, J_{z\pm} = [J_1 + J_2 + J_3 - J_4]/3\sqrt{2}$ and the matrix $\gamma_{\mu\nu}$ in Eq. (3.4). One finally arrives at the most general symmetry-allowed nearest neighbor bilinear spin exchange model on pyrochlore lattice [22] [23]:

$$H = \sum_{\langle ij \rangle} \{ J_{zz} S_i^z S_j^z - J_{\pm}(S_i^+ S_j^- + S_i^- S_j^+) + J_{\pm\pm}[\gamma_{ij} S_i^+ S_j^+ + \gamma_{ij}^* S_i^- S_j^-] + J_{z\pm}[S_i^z(\zeta_{ij} S_j^+ + \zeta_{ij}^* S_j^-) + i \leftrightarrow j] \} \tag{3.6}$$

We consider the case sufficient for pyrochlore compounds with Kramers doublet and map the spin living at the pyrochlore lattice site S_i to the spin defined on the link of dual diamond lattice $S_{\mathbf{r},\mathbf{r}'}$. The site i of the pyrochlore lattice is at the mid point of the link between sites $\mathbf{r}$ and $\mathbf{r}'$ of the dual diamond lattice. Diamond lattice is bipartite lattice formed by two sublattices, which we denote by sublattices I and II, with sites that are the center of up and down tetrahedra respectively. We then use the mapping [24]

$$S_{\mathbf{r}\mathbf{r}'}^+ = \Phi_{\mathbf{r}}^\dagger s_{\mathbf{r}\mathbf{r}'}^+ \Phi_{\mathbf{r}'} = \Phi_{\mathbf{r}}^\dagger e^{iA_{\mathbf{r}\mathbf{r}'}} \Phi_{\mathbf{r}'}, S_{\mathbf{r}\mathbf{r}'}^z = E_{\mathbf{r}\mathbf{r}'} \tag{3.7}$$

to obtain a Hamiltonian describing bosonic spinons, denoted by their creation $\Phi_{\mathbf{r}}^\dagger$ and annihilation $\Phi_{\mathbf{r}}$ operators, hopping between the sites of dual bipartite diamond lattice interacting with compact $U(1)$ gauge field [24]. The $E_{\mathbf{r},\mathbf{r}'}$, taking value $E_{\mathbf{r},\mathbf{r}'} = \pm 1/2$ in the lattice gauge theory, is electric field living at the link of dual diamond lattice, pointing from a center of tetrahedron of pyrochlore lattice at $\mathbf{r}$ to the center of another tetrahedron at $\mathbf{r}'$. It can be represented by arrow along the link in an arrow representation that is popular in 2-d lattice system [78]. Similarly, $\mathbf{A}_{\mathbf{r},\mathbf{r}'} \in [0, 2\pi)$ is lattice compact $U(1)$ gauge field (the lattice version of vector potential of electrodynamics). These two vector operators are conjugate to each other; $[\mathbf{A}, \mathbf{E}] = i$

on the same link and zero otherwise. As such, $\mathbf{A}$ and $\mathbf{E}$ are analogous to momentum $\mathbf{p}$ and position $\mathbf{x}$ respectively and we can thus write $\mathbf{A} = -i\partial/\partial\mathbf{E}$ and $\mathbf{E} = -i\partial/\partial\mathbf{A}$. Being analogous to momentum operator, $\mathbf{A}$ generates operation on quantum state defined by $\mathbf{E}$ analogous to translation generated by momentum;

$$e^{iQA}|E\rangle = |E+Q\rangle \tag{3.8}$$

Their dynamics is described by the Maxwell Hamiltonian [21],

$$H = \frac{U}{2}\sum_{ij} E^2_{\langle ij\rangle} - K\sum_{P}\cos(\nabla\times A)_P \tag{3.9}$$

where the electric field E_{ij} is defined on the link $\langle ij\rangle$ while the gauge field is defined on the links belonging to plaquette P with magnetic flux $B_P = (\nabla\times A)_P = \sum_{ij\in P} A_{ij}$ through the plaquette.

It is also to be noted that the $S^z \leftrightarrow \mathbf{E}$ mapping in Eq. (3.7) reverses the sign of both symmetries under time reversal $\mathcal{T}$ and parity $\mathcal{P}$; S^z is odd under $\mathcal{T}$ and even under $\mathcal{P}$ but $\mathbf{E}$ is even under $\mathcal{T}$ and odd under $\mathcal{P}$. So, the mapping only preserves $\mathcal{T}\times\mathcal{P}$ but not each of $\mathcal{T},\mathcal{P}$ separately.

The lattice boson gauge theory is given by

$$\begin{aligned} H = &\sum_{\mathbf{r}\in \mathrm{I,II}} \frac{J_{zz}}{2} Q^2_{\mathbf{r}} - J_{\pm}\left\{\sum_{\mathbf{r}\in \mathrm{I}}\sum_{\mu,\nu\neq\mu} \Phi^{\dagger}_{\mathbf{r}+\hat{\mathbf{e}}_\mu}\Phi_{\mathbf{r}+\hat{\mathbf{e}}_\nu} s^{-}_{\mathbf{r},\mathbf{r}+\hat{\mathbf{e}}_\mu} s^{+}_{\mathbf{r},\mathbf{r}+\hat{\mathbf{e}}_\nu} + \mathrm{II}\right\} \\ &-J_{z\pm}\left\{\sum_{\mathbf{r}\in \mathrm{I}}\sum_{\mu,\nu\neq\mu} \gamma^{*}_{\mu\nu}\Phi^{\dagger}_{\mathbf{r}}\Phi_{\mathbf{r}+\hat{\mathbf{e}}_\nu} s^{z}_{\mathbf{r},\mathbf{r}+\hat{\mathbf{e}}_\mu} s^{+}_{\mathbf{r},\mathbf{r}+\hat{\mathbf{e}}_\nu} + H.c. + \mathrm{II}\right\} \end{aligned} \tag{3.10}$$

where $\hat{\mathbf{e}}_\mu$ are the local z spin axis unit vectors at the four corners of a tetrahedron of pyrochlore lattice [24], which we will eventually use as the equivalent substitute for global spin space basis vectors [80] and $\gamma_{\mu\nu}$ is element of 4×4 matrix [24]. The vectors $\hat{\mathbf{e}}_\mu$ encode the symmetries of the original microscopic lattice spin model whereas the $\gamma_{\mu\nu}$ matrix encodes the symmetries of the interaction. The $Q_{\mathbf{r}}$ represents the bosonic spinon number operator satisfying commutation relation $[\varphi_{\mathbf{r}}, Q_{\mathbf{r}}] = i$ where $\varphi_{\mathbf{r}}$ is the phase of the bosonic creation operator $\Phi^\dagger_{\mathbf{r}} = e^{i\varphi_{\mathbf{r}}}$. Using gMFT, Savary and Balents [24] have obtained the phase diagram of Eq. (3.10) where $U(1)$ quantum spin liquid phase exists in narrow region in proximity to neighboring magnetically ordered phases.

3.3 Low Energy Effective Theory of Pyrochlore Quantum Spin Ice

In this work, we derive the continuum effective low energy theory of pyrochlore quantum spin ice and investigate the quantum phase transition of $U(1)$ QSL phase of pyrochlore quantum spin ice taking into account gauge fluctuations and the interaction between spinon and photon. The low energy effective field theory is the first main result in this work and is given in Minkowski space-time by [80],

$$S = \int d^4x [\frac{1}{2J_{zz}} |(i\partial_t - e_g A_0)\Phi_{\mathbf{r}}|^2 - \frac{16}{3} J_{\pm} \sum_{\alpha} |(i\partial_\alpha - e_g A_\alpha)\Phi_{\mathbf{r}}|^2 - m|\Phi_{\mathbf{r}}|^2 - u|\Phi_{\mathbf{r}}|^4$$

$$- \frac{1}{2g^2} \sum_{\alpha\beta} (\partial_\alpha A_\beta - \partial_\beta A_\alpha)^2 + \frac{1}{2g^2} \sum_{\alpha} E_\alpha^2] \tag{3.11}$$

with spinon gap m and $\alpha, \beta = x, y, z$. The spin exchange constants J's in the original lattice model Eq. (3.10) determine the coefficients of the field theory. This equation describes complex scalar field coupled to $U(1)$ gauge field. We have explicitly included the Maxwell term originating from Eq. (3.9), separated into its magnetic and electric parts, which describes very well the physics of pyrochlore quantum spin ice. We have written the field theory with parameters in Gaussian unit where $g^2 = \frac{\mu}{\mu_0}$, unit lattice spacing $a = 1$, speed of photon $v_p = 1$ and $\hbar = 1$, but we will revert to physical unit whenever it is necessary.

The field theory Eq. (3.11) is valid low energy description of the pyrochlore quantum spin ice near the minimum of spinon energy dispersion at $\mathbf{k} = 0$, which is the case at mean field level [24] for QSL and AFM phases. The field theory above takes the form of scalar QED [82] [83] with (emergent) $U(1)$ gauge charge $e_g \equiv Q$ where the symbol $\equiv$ means analogy. Physically, $Q = \pm 1$ in the lattice gauge theory Eq. (3.10) but the corresponding charge e_g gives a dimensionless fine structure constant $\alpha_g = e_g^2/(4\pi\varepsilon_0 \hbar v_p)$ that is to be treated as small parameter in field theory Eq. (3.11) as is the case in standard QED [82] [83]. The effective lattice model (3.10) of charged bosons coupled to compact $U(1)$ gauge field has $U(1)$ gauge invariance

representing local gauge charge conservation and the field theory (3.11) preserves this gauge invariance.

This field theory Eq. (3.11) is essentially the quantum ($T = 0$) analog of dynamical Ginzburg-Landau theory of Bardeen-Cooper-Schrieffer (BCS) superconductor where charged matter is coupled to dynamical gauge field. This is also the dynamical version of superconductor under magnetic field [71] with boson density corresponding to Cooper pair density and the gauge field corresponding to the electromagnetic field in such system. This motivates an analogy between the quantum criticality of pyrochlore quantum spin ice described by Eq. (3.11) and classical phase transition in such BCS superconductor under magnetic field.

In type I BCS superconductors, the fluctuations of order parameter field can be neglected because of the narrowness of the temperature interval within which the order parameter fluctuations are important based on Ginzburg criterion [66] [84]. These later fluctuations therefore will not affect significantly the thermodynamics of the transition [71]. For pyrochlore quantum spin ice we suppose that at least for certain compounds, which would really rely on solid state chemistry research, the energy scale interval for the significant effects of order parameter $\langle\Phi\rangle$ quantum fluctuations is much smaller than the critical energy scale regime of the QSL-AFM QPT of interest. Thus order parameter field Φ fluctuations can be neglected and this justifies the approach that we use to derive the quantum free energy to be discussed in Section 3.4 [80]. In this case, the spin exchange J's play the role of energy scale

analogous to temperature T. We discuss in details the derivation of the field theory Eq. (3.11) as follows.

3.3.1 Derivation of Low Energy Effective Theory

We begin with the most general symmetry-allowed nearest neighbor spin exchange model on pyrochlore lattice Eq. (3.6). We now perform the mapping prescribed in Eq. (3.7). Considering the case with $J_{\pm\pm} = 0$ [24], the Hamiltonian of the lattice gauge theory with bosonic spinons defined on the dual diamond bipartite lattice becomes

$$H = \sum_{\mathbf{r}\in \mathrm{I,II}} \frac{J_{zz}}{2} Q_{\mathbf{r}}^2 - J_{\pm} \left\{ \sum_{\mathbf{r}\in \mathrm{I}} \sum_{\mu,\nu\neq\mu} \Phi^{\dagger}_{\mathbf{r}+\hat{\mathbf{e}}_\mu} \Phi_{\mathbf{r}+\hat{\mathbf{e}}_\nu} s^{-}_{\mathbf{r},\mathbf{r}+\hat{\mathbf{e}}_\mu} s^{+}_{\mathbf{r},\mathbf{r}+\hat{\mathbf{e}}_\nu} + \mathrm{II} \right\}$$
$$-J_{z\pm} \left\{ \sum_{\mathbf{r}\in \mathrm{I}} \sum_{\mu,\nu\neq\mu} (\gamma^{*}_{\mu,\nu} \Phi^{\dagger}_{\mathbf{r}} \Phi_{\mathbf{r}+\hat{\mathbf{e}}_\nu} s^{z}_{\mathbf{r},\mathbf{r}+\hat{\mathbf{e}}_\mu} s^{+}_{\mathbf{r},\mathbf{r}+\hat{\mathbf{e}}_\nu} + H.c.) + \mathrm{II} \right\} \tag{3.12}$$

Despite the rather complicated form, the above Hamiltonian has $U(1)$ gauge symmetry, i.e. it is invariant with respect to $U(1)$ gauge transformations $\Phi^{\dagger}_{\mathbf{r}} \to e^{-i\chi(\mathbf{r})}\Phi^{\dagger}_{\mathbf{r}}$, $\Phi_{\mathbf{r}} \to e^{i\chi(\mathbf{r})}\Phi_{\mathbf{r}}$, $A_{\mathbf{r},\mathbf{r}+\hat{\mathbf{e}}_\mu} \to A_{\mathbf{r},\mathbf{r}+\hat{\mathbf{e}}_\mu} + \chi(\mathbf{r}) - \chi(\mathbf{r}+\hat{\mathbf{e}}_\mu)$. The first term is the Ising term expressed in terms of charge $Q_{\mathbf{r}}$ with integer $Q_{\mathbf{r}} \in \mathbb{Z}$ which counts the number of spinons at site $\mathbf{r}$ of the dual diamond lattice.

$$Q_{\mathbf{r}} = \eta_{\mathbf{r}} \sum_{\mu} S^{z}_{\mathbf{r},\mathbf{r}+\eta_{\mathbf{r}}\hat{\mathbf{e}}_\mu} \tag{3.13}$$

where $\eta_{\mathbf{r}} = \pm 1$ for diamond sublattice I(II). In fact, $Q_{\mathbf{r}}$ is the analog of momentum coordinate conjugate to the phase field $\varphi_{\mathbf{r}}$ of $\Phi^{\dagger}_{\mathbf{r}} = e^{i\varphi_{\mathbf{r}}}$ which is analog of the position

coordinate with commutation relation $[\varphi_{\mathbf{r}}, Q_{\mathbf{r}}] = i$. The spinon field is subject to local constraint $|\Phi_{\mathbf{r}}| = 1$.

We take the continuum limit of this lattice gauge theory by performing the following expansion to second order in derivative,

$$\Phi_{\mathbf{r}+\hat{\mathbf{e}}_\mu} = \Phi_{\mathbf{r}} + \hat{\mathbf{e}}_\mu \cdot \nabla \Phi_{\mathbf{r}} + \frac{1}{2}(\hat{\mathbf{e}}_\mu \cdot \nabla)^2 \Phi_{\mathbf{r}} + O(\partial_\mu^3 \Phi) = \Phi_{\mathbf{r}} + \partial_\mu \Phi_{\mathbf{r}} + \frac{1}{2}\partial_\mu^2 \Phi_{\mathbf{r}} + O(\partial_\mu^3 \Phi) \quad (3.14)$$

$$e^{i\int_{\mathbf{r}}^{\mathbf{r}+\hat{\mathbf{e}}_\mu} d\mathbf{r}\cdot\mathbf{A}} = e^{i(\hat{\mathbf{e}}_\mu \cdot \mathbf{A}_{\mathbf{r},\mathbf{r}+\hat{\mathbf{e}}_\mu})} = e^{iA_{\mathbf{r},\mathbf{r}+\hat{\mathbf{e}}_\mu}} = e^{iA_\mu} = 1 + iA_\mu - \frac{1}{2}A_\mu^2 + O(A^3) \quad (3.15)$$

$$A_\nu - A_\mu = A_{\mathbf{r},\mathbf{r}+\hat{\mathbf{e}}_\nu} - A_{\mathbf{r},\mathbf{r}+\hat{\mathbf{e}}_\mu} = A_{\mathbf{r}+\hat{\mathbf{e}}_\mu,\mathbf{r}+\hat{\mathbf{e}}_\nu} = A_{\mathbf{r},\mathbf{r}+\hat{\mathbf{e}}_\nu-\hat{\mathbf{e}}_\mu} = A_{\mathbf{r},\mathbf{r}+\hat{\mathbf{e}}_\delta} = A_\delta \quad (3.16)$$

We have defined $\partial_\mu = \hat{\mathbf{e}}_\mu \cdot \nabla$ and $\hat{\mathbf{e}}_\delta = \hat{\mathbf{e}}_\nu - \hat{\mathbf{e}}_\mu$. With $\mathbf{r}, \mathbf{r}'$ representing the sites of dual diamond lattice, the gauge field $A_{\mathbf{r},\mathbf{r}'}$ lives at the middle of the link $\frac{\mathbf{r}+\mathbf{r}'}{2}$ of dual diamond lattice. At the moment we are essentially working in Gaussian unit such that we have unit lattice spacing $a = 1$, speed of photon $v_p = 1$ and $\hbar = 1$, but we will recover these quantities to their actual physical unit later in the calculation whenever it is necessary.

One may want to compare the treatment of gauge field fluctuations in this gauge theory with that in mean field theory where one assumes a gauge mean field ansatz [24],

$$\langle s^-_\mu \rangle = \frac{1}{2}\cos\theta, \langle s^z_\mu \rangle = \frac{1}{2}\sin\theta\,\varepsilon_\mu \tag{3.17}$$

where $\varepsilon_\mu = (1, 1, -1, -1)$ for $\mu = 0, 1, 2, 3$ corresponding to the four basis vectors of local cubic base of pyrochlore lattice in Eq. (3.3). The QSL state of our interest was found in gMFT to correspond to $\theta = 0$ [24]. We may equally well write an ansatz,

$$\langle s^-_\mu \rangle = \cos\theta, \langle s^z_\mu \rangle = \sin\theta\,\varepsilon_\mu \tag{3.18}$$

Then in the limit $|A_{\mathbf{r},\mathbf{r}'}| = |\int_{\mathbf{r}}^{\mathbf{r}'} \mathbf{A}\cdot d\boldsymbol{r}| \ll 1$, we have

$$s^\pm_{\mathbf{r},\mathbf{r}'} = e^{\pm iA_{\mathbf{r},\mathbf{r}'}} \simeq (1 \pm iA_{\mathbf{r},\mathbf{r}'} - \frac{1}{2}A^2_{\mathbf{r},\mathbf{r}'} + ...)$$

In QSL state, $\cos\theta = 1$ which gives $\langle s^- \rangle = \cos\theta = 1$ and therefore precisely matches with the above expansion for $s^-_{\mathbf{r},\mathbf{r}'}$ at lowest order. Physically, this comparison suggests that the gauge field $A_{\mathbf{r},\mathbf{r}'}$ in our expansion is the gauge fluctuations about the mean field expectation value of gauge field in gMFT [24].

The resulting long wavelength theory (still bearing sublattice sums) is

$$H = \sum_{\mathbf{r}\in \mathrm{I,II}} \frac{J_{zz}}{2} Q^2_{\mathbf{r}}$$

$$-J_\pm \sum_{\mathbf{r}\in \mathrm{I}} \sum_{\mu,\nu\neq\mu} \left\{\Phi^\dagger_{\mathbf{r}}\Phi_{\mathbf{r}} + \Phi^\dagger_{\mathbf{r}}(\partial_\nu\Phi_{\mathbf{r}}) + (\partial_\mu\Phi^\dagger_{\mathbf{r}})\Phi_{\mathbf{r}} + \ldots\right\}\left(1 + iA_\delta - \frac{1}{2}A^2_\delta + \ldots\right)$$

$$-J_\pm \sum_{\mathbf{r}\in \mathrm{II}} \sum_{\mu,\nu\neq\mu} \left\{\Phi^\dagger_{\mathbf{r}}\Phi_{\mathbf{r}} - \Phi^\dagger_{\mathbf{r}}(\partial_\nu\Phi_{\mathbf{r}}) - (\partial_\mu\Phi^\dagger_{\mathbf{r}})\Phi_{\mathbf{r}} + \ldots\right\}\left(1 - iA_\delta - \frac{1}{2}A^2_\delta + \ldots\right)$$

$$-J_{z\pm}\left\{\sum_{\mathbf{r}\in \mathrm{I}}\sum_{\mu,\nu\neq\mu}(\Phi^{\dagger}_{\mathbf{r}}\Phi_{\mathbf{r}}+\Phi^{\dagger}_{\mathbf{r}}\partial_{\nu}\Phi_{\mathbf{r}}+\frac{1}{2}\Phi^{\dagger}_{\mathbf{r}}\partial^{2}_{\nu}\Phi_{\mathbf{r}}+...)E_{\mu}(1+iA_{\nu}-\frac{1}{2}A^{2}_{\nu}+...)+H.c\right\}$$
$$-J_{z\pm}\left\{\sum_{\mathbf{r}\in \mathrm{II}}\sum_{\mu,\nu\neq\mu}(\Phi^{\dagger}_{\mathbf{r}}\Phi_{\mathbf{r}}-\partial_{\nu}\Phi^{\dagger}_{\mathbf{r}}\Phi_{\mathbf{r}}+\frac{1}{2}\partial^{2}_{\nu}\Phi^{\dagger}_{\mathbf{r}}\Phi_{\mathbf{r}}+...)E_{\mu}(1+iA_{\nu}-\frac{1}{2}A^{2}_{\nu}+\ldots)+H.c\right\} \tag{3.19}$$

where we have denoted $A_{\mu}=A_{\mathbf{r},\mathbf{r}+\hat{\mathbf{e}}_{\mu}}$ in sublattice I and $A_{\mu}=A_{\mathbf{r},\mathbf{r}-\hat{\mathbf{e}}_{\mu}}$ in sublattice II. Likewise, $E_{\mu}=E_{\mathbf{r},\mathbf{r}+\hat{\mathbf{e}}_{\mu}}$ in sublattice I and $E_{\mu}=E_{\mathbf{r},\mathbf{r}-\hat{\mathbf{e}}_{\mu}}$ in sublattice II. The electric field is $E_{\mu}=-\partial_{\mu}A_{0}-\partial_{t}A_{\mu}=-\partial_{t}A_{\mu}$. The $\mathbf{r},\mathbf{r}'=\mathbf{r}\pm\hat{\mathbf{e}}_{\mu}$ here denotes direction of vector to be pointing from $\mathbf{r}$ to $\mathbf{r}'=\mathbf{r}\pm\hat{\mathbf{e}}_{\mu}$. For the last terms involving coupling $J_{z\pm}$, we will retain only the lowest order terms in derivatives and gauge fields, valid in the low energy long distance limit, which must preserve gauge invariance of the microscopic model Eq. (3.12).

With $\Phi^{\dagger}_{\mathbf{r}}=e^{i\varphi_{\mathbf{r}}}$ and using commutation relation $[\varphi_{\mathbf{r}},Q_{\mathbf{r}}]=i$, we can write $Q_{\mathbf{r}}=\frac{1}{i}\frac{\partial}{\partial\varphi_{\mathbf{r}}},\varphi_{\mathbf{r}}=\frac{1}{i}\frac{\partial}{\partial Q_{\mathbf{r}}}$. It can be shown that the term $Q^{2}_{\mathbf{r}}$ can be written as $Q^{2}_{\mathbf{r}}=t_{s}^{2}\frac{d\Phi^{*}_{\mathbf{r}}}{dt}\frac{d\Phi_{\mathbf{r}}}{dt}$ in the field theory language where t_s is an appropriate time scale needed to get the dimension right. This time scale is $t_s=\frac{\hbar}{J_{zz}}(\equiv\frac{1}{J_{zz}}$ in Gaussian unit) because the coupling J_{zz} is the reference energy scale (coupling constant) in the phase diagram. One may want to minimally couple this term to the the scalar potential A_0 to get gauge invariant term $Q^{2}_{\mathbf{r}}=|(i\partial_{t}-A_{0})\Phi_{\mathbf{r}}|^{2}$ but we may make gauge choice $A_0=0$ and only vector potential $\mathbf{A}$ exists with the electric field $\mathbf{E}$ coming entirely from this vector potential.

We obtain from Eq. (3.19) a 3+1-D continuum action in real (Minkowskian) time

$(T = 0)$ field theory [82] [83],

$$S = \int d^4x [\frac{1}{2J_{zz}} |(i\partial_t - e_g A_0)\Phi_{\mathbf{r}}|^2 - \frac{1}{2} J_{\pm} \sum_{\mu,\nu\neq\mu} |(i\partial_\delta - eA_\delta)\Phi_{\mathbf{r}}|^2 - (\lambda - 12J_{\pm})|\Phi_{\mathbf{r}}|^2$$
$$- \frac{1}{2g^2} \sum_{\alpha\beta} (\partial_\alpha A_\beta - \partial_\beta A_\alpha)^2 + \frac{1}{2g^2} \sum_{\alpha} E_\alpha^2 + \frac{1}{2} J_{z\pm} \{ \sum_{\mu,\nu\neq\mu} \gamma^*_{\mu\nu} ieE_\mu J_\nu + H.c. \}$$
$$- \frac{1}{2} J_{z\pm} \sum_{\mu,\nu\neq\mu} \{\gamma^*_{\mu\nu} eE_\mu |(i\partial_\nu - eA_\nu)\Phi_{\mathbf{r}}|^2 + H.c.\}] \tag{3.20}$$

with the gauge invariant Noether current J_ν given by

$$J_\nu = \Phi^*_{\mathbf{r}}(-i\partial_\nu + eA_\nu)\Phi_{\mathbf{r}} + \Phi_{\mathbf{r}}(i\partial_\nu + eA_\nu)\Phi^*_{\mathbf{r}} \tag{3.21}$$

and the partition function

$$Z = \int \mathcal{D}\Phi^* \mathcal{D}\Phi \mathcal{D}A \mathcal{D}\lambda e^{iS[\Phi^*,\Phi,A,\lambda]}$$

where we have added the Lagrange multiplier term. Strictly speaking, the constraint $|\Phi_{\mathbf{r}}| = 1$ should be imposed locally by using Lagrange multiplier term $\int d^4x\, \lambda_{\mathbf{r}}(\Phi^*_{\mathbf{r}}\Phi_{\mathbf{r}} - 1)$ with $\lambda_{\mathbf{r}} > 0$. However, we relax this constraint by using global Lagrange multiplier term $\lambda \int d^4x\, (\Phi^*_{\mathbf{r}}\Phi_{\mathbf{r}} - 1)$ that globally imposes the Hilbert space constraint on the spinon field $|\Phi_{\mathbf{r}}| = 1$ so that we can use constant (spatially uniform) variable λ [24]. The $\lambda \int d^4x(-1)$ piece contributes only a constant energy shift and is omitted from Eq. (3.20). The Hermitian conjugation operation (†) in the original Hamiltonian language becomes simply complex conjugation operation (*) in the field theory language as

the original bosonic spinon creation and annihilation operators now simply become complex scalar field.

The $\mu, \nu = 0, 1, 2, 3$ are the indices of local z spin axes $\hat{\mathbf{e}}_{\mu(\nu)}$ and $\alpha, \beta = x, y, z$. The mass parameter $m = \lambda - 12J_{\pm}$ is the spinon gap. We do not compute explicitly the value of Lagrange multiplier λ in this low energy effective theory description. However, it has been computed at mean field level in [24] where the value of λ crucially determines the phases and phase transition in the phase diagram. Direct comparison with the result in [24] for the QSL-AFM phase transition of interest here gives

$$\lambda = \frac{3}{2} J_{zz} \left(\int_{\mathbf{k}} \frac{1}{\sqrt{3 - \frac{1}{2} L_{\mathbf{k}}}} \right)^2 \tag{3.22}$$

where $L_{\mathbf{k}}$ is the geometric factor $L_{\mathbf{k}} = \sum_{\mu,\nu<\mu} \cos[\mathbf{k} \cdot (\hat{\mathbf{e}}_{\mu} - \hat{\mathbf{e}}_{\nu})]$. We see that the spinon gap is linearly proportional to the Ising coupling J_{zz}. This completely agrees with the fact that spinon is created by flipping of Ising spin out of or into the center of pyrochlore tetrahedron with energy cost of order $\sim J_{zz}$. This observation thus gives a reassuring check of the correctness of our low energy effective theory.

We have included in the Eq. (3.20) the free Maxwell term of Abelian $U(1)$ gauge theory, separated into its magnetic field and electric field parts, analogous to the Maxwell term of QED: $-\frac{1}{4} F_{\mu\nu} F^{\mu\nu}$ in Gaussian unit, with $\mu = g^2 \mu_0$. This free Maxwell action corresponds to $-\frac{1}{2} \left(c^2 \mathbf{B}^2 - \mathbf{E}^2 \right)$ which is standard in $U(1)$ gauge theory. This term corresponds directly to the lattice Maxwell Hamiltonian in Eq. (3.9). In the

limit of small $\nabla \times A$, we can expand the cosine and obtain, omitting the uninteresting constant term,

$$H = \frac{U}{2} \sum_{ij} E_{ij}^2 + \frac{K}{2} \sum_{P} (\nabla \times A)_P^2 \tag{3.23}$$

The first and second terms are nothing but the electric field and magnetic field terms of the usual Maxwell Lagrangian. This gives photon speed $v_p = \sqrt{K/U}$. The photon speed is determined by K and U, which should depend on the microscopic parameters of material. We have also included the emergent $U(1)$ gauge charge $e_g \equiv Q$ (or equivalently e which we define as $e = \frac{4}{3} e_g$) together with each of the gauge fields A and E which represents the strength of spinon-gauge field coupling.

The field theory in Eq. (3.20), apart from the last two terms, is called scalar QED in QFT. This scalar QED part is truly Lorentz invariant when the speed of spinon $v_s = \sqrt{32 J_{zz} J_{\pm}/3}$ equals the photon speed $v_p = \sqrt{K/U}$. The last two terms in Eq. (3.20) are novel terms that reflect the unique physics of field theory of pyrochlore quantum spin ice, derived directly from the effective lattice model Eq. (3.12). We treat these last two terms as perturbation to the scalar QED part. This is justified by the fact that these last two terms have coupling proportional to $U(1)$ gauge charge e (or equivalently e_g) and because these terms are linear in electric field, they should be multiplied with an inverse of mass scale in order to have proper mass dimension. This mass scale is nothing but a UV cut off Λ; a large momentum (mass) scale which we can take as the inverse of the small lattice spacing a. Further, these last two terms give

rise to several new types of vertex; the simplest ones being scalar-scalar-gauge field vertex and scalar-scalar-gauge field-gauge field vertex. However, we will not discuss the renormalization effect of these terms or explicitly compute their contribution to the renormalization correction of the appropriate terms of the scalar QED but only give the order of magnitude of those corrections. The two most important renormalization effects of those vertices are mass renormalization and quartic term renormalization. Denoting them as $\delta m^{z\pm}$ and $\delta u^{z\pm}$ respectively, it is easy to check that the leading contributions are $\delta m^{z\pm} = \mathcal{O}(e^2 J_{z\pm}^2)$ and $\delta u^{z\pm} = \mathcal{O}(e^4 J_{z\pm}^2)$.

The new field theory upon taking the above consideration now becomes

$$S = \int d^4x [\frac{1}{2J_{zz}} |(i\partial_t - e_g A_0)\Phi_{\mathbf{r}}|^2 - \frac{16}{3} J_{\pm} \sum_{\alpha} |(i\partial_\alpha - e_g A_\alpha)\Phi_{\mathbf{r}}|^2 - m|\Phi_{\mathbf{r}}|^2 - u|\Phi_{\mathbf{r}}|^4 - \frac{1}{2g^2} \sum_{\alpha\beta} (\partial_\alpha A_\beta - \partial_\beta A_\alpha)^2 + \frac{1}{2g^2} \sum_{\alpha} E_\alpha^2] \tag{3.24}$$

where we have used the mapping Eq. (3.5) and the gauge field mapping to express all the vectors in global Cartesian coordinate basis.

$$\mathcal{A}_\mu(\mathbf{r}) = \frac{3}{4} \sum_{\alpha} n_{\mu\alpha} A_\alpha(\mathbf{r}) = \frac{3}{4} \sum_{\alpha} (\hat{\mathbf{e}}_\mu \cdot \hat{\mathbf{e}}_\alpha) A_\alpha(\mathbf{r}) \tag{3.25}$$

where it is understood that $\mathcal{A}_\mu(\mathbf{r}) \equiv \mathcal{A}(\mathbf{r} + \frac{\hat{\mathbf{e}}_\mu}{2})$ in lattice corresponds to continuum gauge field $\mathbf{A}(\mathbf{r})$ defined at $\mathbf{r}$ pointing along the direction of $\hat{\mathbf{e}}_\mu$ with (α, β) represents the index of global orthogonal basis vectors of 3-d space $(\hat{\mathbf{x}}, \hat{\mathbf{y}}, \hat{\mathbf{z}})$ while (μ, ν) labels the non-orthogonal local cubic basis vectors $(\hat{\mathbf{e}}_0, \hat{\mathbf{e}}_1, \hat{\mathbf{e}}_2, \hat{\mathbf{e}}_3)$ defined in Eq. (3.3).

In passing, we note that the resulting effective action Eq. (3.20) contains current-electric field coupling

$$S_{E-J} = \frac{1}{2} J_{z\pm} \{ \sum_{\mu,\nu\neq\mu} \gamma^*_{\mu\nu} ieE_\mu J_\nu + H.c. \}$$

Written in terms of x, y and z components, it takes the form

$$S_{E-J} = \frac{1}{2} J_{z\pm} e(E_y J_y - E_z J_z + H.c. \}$$

We see that rather than having rotationally symmetric $\mathbf{J} \cdot \mathbf{E}$ (or $J^\mu E_\mu$ in its relativistic version), we have this asymmetric form. The local environments possess special directions, namely the three-fold rotational axes pointing along 111. These are chosen as the local z axes. The z axes clearly respects the cubic symmetry: rotations preserving the pyrochlore lattice transform one z axis into another. The same cannot be done with local frames, which have, in addition to the aforementioned z axes, x and y (orthogonal to each other and to z). No matter how the local x and y axes are chosen, not all point-group transformations will turn one triplet (x,y,z) into another. One can start with some orientation of the local frame on one vertex of a tetrahedron (say, 0) and apply three rotations to generate the frames on the other three (1, 2, and 3). However, a rotation that takes vertex 1 into 2 will not turn the (x,y,z) frame at 1 into the (x,y,z) frame at 2. The z axis will be rotated correctly, but the x and y will not. This can be directly tied to the non-Abelian nature of SO(3). This asymmetry thus originates from the impossibility to set four rotational frames (each consisting

of three orthogonal axes) in the corners of a regular tetrahedron that would respect the rotational symmetries of the tetrahedral group. This is related to the noncommutativity of rotational operators. We do not intend to pursue the physical meaning or consequences of this asymmetry further. This asymmetric $\mathbf{E}-\mathbf{J}$ term clearly also breaks rotational symmetry but as stated earlier, we take the effect of this term as perturbative effect.

3.4 Free Energy Description of $U(1)$ QSL-AFM QPT

The QSL to AFM phase transition can be described by an effective action in terms of bosonic spinon field expectation value $\langle\Phi\rangle$ (as the order parameter, in the language of Landau symmetry breaking). To arrive at that, we formally integrate out the gauge fields from our full action using both static spatially uniform (mean-field) solution approximation [71] and functional integration [81].

$$\begin{aligned} Z &= \int \mathcal{D}\Phi^* \int \mathcal{D}\Phi \int \mathcal{D}\lambda \int \mathcal{D}A e^{-S[\Phi^*,\Phi,\lambda,A]} \\ &= \int \mathcal{D}\Phi^* \int \mathcal{D}\Phi e^{-S_{eff}[\Phi^*,\Phi]} = \int \mathcal{D}\Phi^* \int \mathcal{D}\Phi e^{-\frac{F[\Phi^*,\Phi]}{T_{QPT}}} \end{aligned} \tag{3.26}$$

We obtain the "free energy" (the quantum version analog of classical thermal free energy) of bosonic spinon fields $F[\Phi^*_{\mathbf{r}}, \Phi_{\mathbf{r}}]$ with $J_\pm$ playing the role of energy scale

T_{QPT} that tunes the QSL-AFM quantum phase transition [80],

$$F[\Phi^*_{\mathbf{r}}, \Phi_{\mathbf{r}}] = \int d^3r [c_2|\Phi_{\mathbf{r}}|^2 - c_3|\Phi_{\mathbf{r}}|^3 + c_4|\Phi_{\mathbf{r}}|^4] \tag{3.27}$$

The coefficients in physical unit are $c_2 = m + \delta m$ with $m = \lambda - 12J_\pm$, $\delta m = \frac{16J_\pm a^2 e_g^2 g^2 \mu_0 J^c_\pm \Lambda}{\pi^2\hbar^2} + \mathcal{O}(e_g^2 J^2_{z\pm})$, $c_3 = \frac{16J_\pm a^2 e_g^2 g^2 \mu_0 J^c_\pm}{3\pi\hbar^2}\sqrt{\frac{32J_\pm a^2 e_g^2 g^2 \mu_0}{3\hbar^2}}$ and $c_4 \equiv u = u_0 + \mathcal{O}(J^2_{z\pm} e_g^4)$. $J^c_\pm = \lambda/12$ is the critical $J_\pm$ at which m changes sign whereas $\Lambda \sim 1/a$ with a is microscopic lattice spacing [80]. The last correction to δm given by its order of magnitude $\mathcal{O}(e_g^2 J^2_{z\pm})$ and the correction to quartic coefficient $\mathcal{O}(e_g^4 J^2_{z\pm})$ come from novel terms with coupling constant proportional to $J_{z\pm}$ which we treat as perturbation and give rise to loop corrections to the appropriate terms in the scalar QED; quadratic (mass) and quartic terms respectively in the field theory Eq. (3.11). These loop corrections do not change the final conclusions of this work qualitatively.

Quartic term is needed from the beginning to ensure both the stability and the renormalizability of the field theory. Microscopically in the context of this work, it can be provided by the $J_{\pm\pm}[\gamma_{ij} S_i^+ S_j^+ + \gamma^*_{ij} S_i^- S_j^-]$ term in the microscopic spin model [24], where in this case $u_0 \sim J_{\pm\pm}$. But including such term will give rise to a slightly different mean field phase diagram with $U(1)$ QSL and antiferromagnetic quadrupolar (AFQ) order [79] compared to AFM for the case with $J_{\pm\pm} = 0$ [24]. We may however consider the case with very small $J_{\pm\pm} \ll J_\pm$, $J_{z\pm} < J_{zz}$ which is sufficient to ensure the stability of the field theory describing the phase transition and yet can still be used to describe phase diagram with $J_{\pm\pm} = 0$ [24]. From more

general perspective, spin exchange model of the form $J_{ij}^{ab} S_i^a S_j^b$ followed by slave-particle type decomposition $S_i^a = \frac{1}{2}\Phi_{i\alpha}^\dagger \sigma_{\alpha\beta}^a \Phi_{i\beta}$ will in general generate quartic term from the product of two spin operators which gives rise to product of four spinon operators and in this case $u_0 \sim J_{ij}^{ab}$ as a result.

This free energy Eq. (3.27) is the second main result in this work. We note that the coupling to gauge field generates the crucial cubic term with negative coefficient which gives rise to first order phase transition with order parameter $\langle\Phi\rangle$ as we change the coupling $J_\pm$ while $J_{z\pm}$ mainly gives rise to corrections to spinon gap (mass) and especially to quartic term which ensures the stability of the theory. Increasing $J_\pm$ with other parameters fixed drives bosonic spinon condensation and this describes the QSL to AFM quantum phase transition.

The location of QSL-AFM phase transition can be predicted directly from the free energy Eq. (3.27) which can be shown to suggest that the phase transition occurs at $c_2 = \frac{c_3^2}{4c_4}$. Physically, the QSL to AFM phase transition is bosonic spinon condensation that occurs once the spinon becomes gapless. To lowest order approximation, the free energy Eq. (3.27) predicts the QSL to AFM transition to occur at $\lambda \simeq 3J_\pm$ [80], the third main result in this work, in precise agreement with Ref. [24].

A quantity of interest in a first order phase transition is the size of that transition. From the free energy Eq. (3.27), we define the size of first order transition η as the ratio of the shift in critical energy scale between that of second order phase transition when no coupling to gauge field exists and that of first order phase transition upon

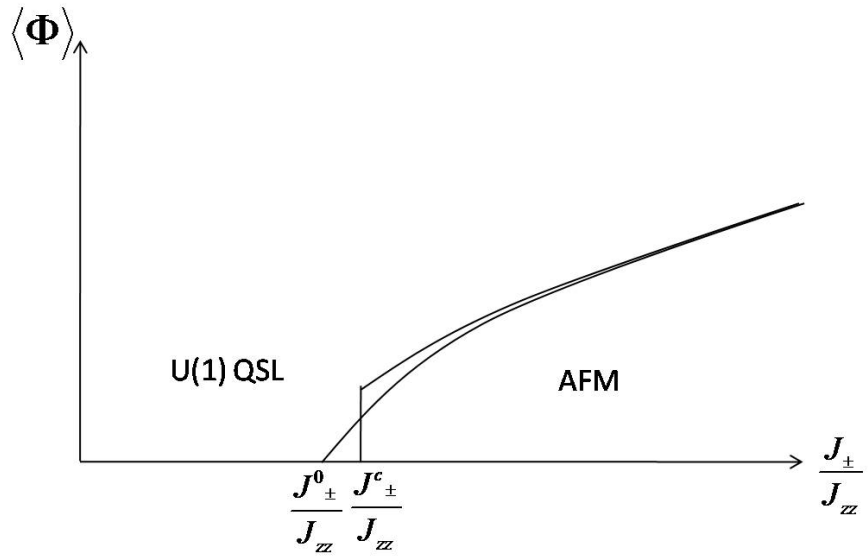

Figure 3.3: Illustration of the process of fluctuation-induced first order phase transition between $U(1)$ QSL and AFM phases of pyrochlore quantum spin ice.

coupling to gauge field to the original critical energy scale of the second order phase transition. We obtain $\eta = \frac{J_{\pm}^{c\,\prime} - J_{\pm}^{c}}{J_{\pm}^{c}} \sim \frac{a e_g^2 g^2 \mu_0 J_{\pm}^{c}}{\hbar^2}$. The numerical value of this quantity depends on the gauge charge e_g and permeability ratio g which should be determined empirically. A trial estimate using standard QED parameters gives $\eta \sim 10^{-8}$, which suggests a very weak first order phase transition. Actual value for η should be larger than this estimate, but still puts the phase transition as weakly first order [80]. This is the final main result of this work.

We have therefore shown that the gauge field fluctuations have driven the mean field second order continuous QSL to AFM quantum phase transition to weakly first order phase transition. An analogy with the classical thermal fluctuation-induced first order phase transitions requires a coupling of an order parameter to gauge field to drive the phase transition to first order. In our work, such order parameter is

the expectation value of bosonic spinon field which appears in mean field decomposition of the lattice gauge theory Eq. (3.10); $\langle\Phi^\dagger\Phi\rangle = \langle|\Phi|^2\rangle = |\langle\Phi\rangle|^2 + \langle|\Delta\Phi|^2\rangle$. This mechanism is possible because the spinons carry emergent $U(1)$ gauge charge that couple to emergent electromagnetic gauge field $\mathbf{A}$, that is, it all arises from the $U(1)$ gauge structure of the theory with complex scalar field coupling to the $U(1)$ gauge field via the $U(1)$ gauge charge. However, different from previous studies at finite temperatures or low temperatures near quantum critical point, in this work the phase transition is between zero temperature ground states with quantum rather than thermal fluctuations.

3.4.1 Free Energy Derivation for QSL-AFM QPT

In this subsection, we give the details of the derivation of (quantum analog of the classical thermal) "free energy" for bosonic spinon fields to be used to describe QSL-AFM quantum phase transition where the expectation value of spinon field $\langle\Phi\rangle$ is the order parameter for this transition. We also show in detail the derivation of several results characterizing the properties of the phase transition.

The field theory for pyrochlore quantum spin ice in imaginary time (Euclidean space-time) [81] with $t = -i\tau$ is described by

$$S^E = \int d^4x^E [\frac{1}{2J_{zz}}|(\partial_\tau + ie_g A_0)\Phi_{\mathbf{r}}|^2 + \frac{16}{3}J_\pm \sum_\alpha |(\partial_\alpha + ie_g A_\alpha)\Phi_{\mathbf{r}}|^2 + m|\Phi_{\mathbf{r}}|^2 + u|\Phi_{\mathbf{r}}|^4$$

$$+\frac{1}{2g^2}\sum_{\alpha\beta}(\partial_\alpha A_\beta - \partial_\beta A_\alpha)^2 + \frac{1}{2g^2}\sum_\alpha E_\alpha^2] \tag{3.28}$$

We aim for free energy $F[\Phi^*, \Phi]$ to describe the QSL-AFM phase transition because such transition is based on bosonic spinon condensation where $\langle\Phi\rangle = 0$ in QSL and $\langle\Phi\rangle \neq 0$ in AFM. It is to be noted in both of these phases, $\langle E\rangle = 0$ [24]. From Eq. (3.28), the real space free energy density of spinon in the static spatially uniform approximation [71], obtained by taking $\partial_\alpha \Phi_{\mathbf{r}} = 0$, gives

$$\begin{aligned}\frac{1}{V}\frac{\delta F[\Phi^*_{\mathbf{r}}, \Phi_{\mathbf{r}}]}{\delta|\Phi_{\mathbf{r}}|} &= 2m|\Phi_{\mathbf{r}}| + 4u|\Phi_{\mathbf{r}}|^3 + J_\pm e^2 \sum_{\mu,\nu\neq\mu}\langle A^2_\delta(\mathbf{r})\rangle_\Phi |\Phi_{\mathbf{r}}| \\ &= 2m|\Phi_{\mathbf{r}}| + 4u|\Phi_{\mathbf{r}}|^3 + 6J_\pm e^2 \sum_{\alpha\beta}\langle A_\alpha(\mathbf{r})A_\beta(\mathbf{r})\rangle_\Phi \delta_{\alpha\beta}|\Phi_{\mathbf{r}}|\end{aligned} \tag{3.29}$$

where V is the system volume. The expectation value $\langle\ldots\rangle$ in Eq. (3.29) is evaluated with respect to appropriate action. The next step is therefore to compute these expectation values. Taking Fourier transform, we have to compute $\langle A_{\delta(\mathbf{k}'')}A_{\delta(\mathbf{k}''')}\rangle_\Phi$ which is the expectation value of $A_{\delta(\mathbf{k}'')}A_{\delta(\mathbf{k}''')}$ with respect to the action (free energy) of A taken at constant spatially uniform value of Φ.

$$\begin{aligned}\langle A_{\delta(\mathbf{k}'')}A_{\delta(\mathbf{k}''')}\rangle_\Phi &= \frac{\int \mathcal{D}\mathbf{A} e^{-\frac{F[\mathbf{A}]_\Phi}{T_{QPT}}} A_{\delta(\mathbf{k}'')}A_{\delta(\mathbf{k}''')}}{\int \mathcal{D}\mathbf{A} e^{-\frac{F[\mathbf{A}]_\Phi}{T_{QPT}}}} \\ &= \sum_{\alpha\beta}\left(\frac{3}{4}\right)^2 n_{\delta\alpha}n_{\delta\beta}\frac{\int \mathcal{D}\mathbf{A} e^{-\frac{F[\mathbf{A}]_\Phi}{T_{QPT}}} A_{\alpha(\mathbf{k}'')}A_{\beta(\mathbf{k}''')}}{\int \mathcal{D}\mathbf{A} e^{-\frac{F[\mathbf{A}]_\Phi}{T_{QPT}}}} \\ &= \left(\frac{3}{4}\right)^2 \sum_{\alpha\beta} n_{\delta\alpha}n_{\delta\beta}\langle A_{\alpha(\mathbf{k}'')}A_{\beta(\mathbf{k}''')}\rangle_\Phi\end{aligned}$$

with the coefficient $n_{\delta\alpha} = (\hat{\mathbf{e}}_\nu - \hat{\mathbf{e}}_\nu) \cdot \hat{\mathbf{e}}_\alpha$ as defined following Eq. (3.5). Here, the coupling $J_\pm$ plays the role of energy scale T_{QPT} that tunes this quantum phase transition. The free energy of the gauge field is

$$\begin{aligned} F[\mathbf{A}]_\Phi &= \frac{1}{2g^2} \int_{\mathbf{k}'',\mathbf{k}'''} A_{\alpha(\mathbf{k}'')}(\mathbf{k}''^2 \delta_{\alpha\beta} - k''_\alpha k''_\beta) A_{\beta(\mathbf{k}''')} \delta(\mathbf{k}'' + \mathbf{k}''') \\ &+ \frac{1}{2} J_\pm \sum_{\mu,\nu\neq\mu} \int_{\mathbf{k},\mathbf{k}',\mathbf{k}'',\mathbf{k}'''} e^2 A_{\delta(\mathbf{k}'')} A_{\delta(\mathbf{k}''')} \langle \Phi^*_{\mathbf{k}} \Phi_{\mathbf{k}'} \rangle \delta(-\mathbf{k} + \mathbf{k}' + \mathbf{k}'' + \mathbf{k}''') \\ &= \frac{1}{2g^2} \int_{\mathbf{k}'',\mathbf{k}'''} A_{\alpha(\mathbf{k}'')}(\mathbf{k}''^2 \delta_{\alpha\beta} - k''_\alpha k''_\beta) A_{\beta(\mathbf{k}''')} \delta(\mathbf{k}'' + \mathbf{k}''') \\ &+ 3 J_\pm \sum_{\alpha\beta} \int_{\mathbf{k},\mathbf{k}',\mathbf{k}'',\mathbf{k}'''} e^2 A_{\alpha(\mathbf{k}'')} A_{\beta(\mathbf{k}''')} \langle \Phi^*_{\mathbf{k}} \Phi_{\mathbf{k}'} \rangle \delta(-\mathbf{k} + \mathbf{k}' + \mathbf{k}'' + \mathbf{k}''') \end{aligned} \tag{3.30}$$

with $\delta(\mathbf{k})$ is the Dirac delta function. In this free energy language, each $\int_{\mathbf{k}}$ is 3-d momentum integral $\int \frac{d^3k}{(2\pi)^3}$. We also have used

$$\begin{aligned} \sum_{\mu,\nu\neq\mu} A_{\delta(\mathbf{k}'')} A_{\delta(\mathbf{k}''')} &= \left(\frac{3}{4}\right)^2 \sum_{\mu,\nu\neq\mu} \sum_{\alpha\beta} n_{\delta\alpha} A_{\alpha(\mathbf{k}'')} n_{\delta\beta} A_{\beta(\mathbf{k}''')} \\ &= 6 \sum_{\alpha\beta} A_{\alpha(\mathbf{k}'')} A_{\beta(\mathbf{k}''')} \delta_{\alpha\beta} \end{aligned} \tag{3.31}$$

Noting that $\langle \Phi^*_{\mathbf{k}} \Phi_{\mathbf{k}'} \rangle \sim \delta(\mathbf{k}' - \mathbf{k})$ and using

$$\begin{aligned} Z_{\mathbf{A}} &= \int \mathcal{D}\mathbf{A} e^{-\int_{\mathbf{k}'',\mathbf{k}'''} A_{\alpha(\mathbf{k}'')} M^\Phi_{\alpha\beta}(\mathbf{k}'',\mathbf{k}''') A_{\beta(\mathbf{k}''')} \delta(\mathbf{k}''+\mathbf{k}''')} \\ &= \int \mathcal{D}\mathbf{A} e^{-S[\mathbf{A}]} = \frac{1}{M^\Phi_{\alpha\beta}} \delta(\mathbf{k}'' + \mathbf{k}''') \end{aligned} \tag{3.32}$$

and

$$\begin{aligned}\langle A_{\alpha(\mathbf{k}'')}A_{\beta(\mathbf{k}''')}\rangle &= \frac{\int \mathcal{D}\mathbf{A}e^{-S[\mathbf{A}]}A_{\alpha(\mathbf{k}'')}A_{\beta(\mathbf{k}''')}}{\int \mathcal{D}\mathbf{A}e^{-S[\mathbf{A}]}} \\ &= -\frac{1}{Z_{\mathbf{A}}}\frac{\partial Z_{\mathbf{A}}}{\partial M^{\Phi}_{\alpha\beta}} = \frac{1}{M^{\Phi}_{\alpha\beta}}\delta\left(\mathbf{k}''+\mathbf{k}'''\right)\end{aligned} \tag{3.33}$$

, the result is

$$\langle A_{\alpha(\mathbf{k}'')}A_{\beta(\mathbf{k}''')}\rangle_{\Phi} = \frac{2g^2J^c_{\pm}}{\mathbf{k}''^2+6J_{\pm}e^2g^2|\Phi|^2}\left(\delta_{\alpha\beta}-\frac{k''_{\alpha}k''_{\beta}}{\mathbf{k}''^2}\right)\delta_{\mathbf{k}'',-\mathbf{k}'''} \tag{3.34}$$

and so

$$\begin{aligned}&\langle A_{\delta(\mathbf{k}'')}A_{\delta(\mathbf{k}''')}\rangle_{\Phi} = \\ &\left(\frac{3}{4}\right)^2\sum_{\alpha\beta}\frac{2g^2J^c_{\pm}n_{\delta\alpha}n_{\delta\beta}}{\mathbf{k}''^2+6J_{\pm}e^2g^2|\Phi|^2}\left(\delta_{\alpha\beta}-\frac{k''_{\alpha}k''_{\beta}}{\mathbf{k}''^2}\right)\delta_{\mathbf{k}'',-\mathbf{k}'''}\end{aligned} \tag{3.35}$$

where $J^c_{\pm}=\lambda/12$ is the critical $J_{\pm}$ at which m changes sign. Retaining only the gauge independent part of the transverse projector, as only this part that should contribute to physical process, we have

$$\frac{1}{V}\frac{\delta F[\Phi^*_{\mathbf{r}},\Phi_{\mathbf{r}}]}{\delta|\Phi_{\mathbf{r}}|} = 2m|\Phi_{\mathbf{r}}|+4u|\Phi_{\mathbf{r}}|^3+6J_{\pm}e^2\sum_{\alpha\beta}\int_{\mathbf{k}''}\frac{2g^2J^c_{\pm}}{\mathbf{k}''^2+6J_{\pm}e^2g^2|\Phi|^2}\delta_{\alpha\beta}|\Phi_{\mathbf{r}}| \tag{3.36}$$

where we have used $\sum_{\mu,\nu\neq\mu}n_{\delta\alpha}n_{\delta\beta}=\frac{32}{3}\delta_{\alpha\beta}$ to obtain the last line. The integral $\int_{\mathbf{k}''}\frac{2g^2J^c_{\pm}}{\mathbf{k}''^2+6J_{\pm}e^2g^2|\Phi|^2}\delta_{\alpha\beta}$ is UV divergent and so we impose UV cut-off. Denoting $k_s^2=6J_{\pm}e^2g^2|\Phi|^2$, we obtain

$$\int\frac{d^3k''}{(2\pi)^3}\frac{1}{\mathbf{k}''^2+k_s^2} = \frac{1}{(2\pi)^3}4\pi\left(\Lambda-k_s\arctan[\frac{\Lambda}{k_s}]\right)$$

$$\simeq \frac{1}{2\pi^2}\left(\Lambda - \frac{\pi}{2}k_s\right) \tag{3.37}$$

in the limit of large Λ/k_s. To obtain the final free energy density in real space, we recover the spatial dependence of the Φ and impose locality of the free energy and get

$$\frac{1}{V}\frac{\delta F[\Phi^*_{\mathbf{r}}, \Phi_{\mathbf{r}}]}{\delta|\Phi_{\mathbf{r}}|} = 2m|\Phi_{\mathbf{r}}| + 4u|\Phi_{\mathbf{r}}|^3 + \frac{6e^2g^2}{\pi^2}J_\pm J^c_\pm(\Lambda - \frac{\pi}{2}\sqrt{6J_\pm e^2g^2|\Phi_{\mathbf{r}}|^2})\sum_{\alpha\beta}\delta_{\alpha\beta}|\Phi_{\mathbf{r}}| \tag{3.38}$$

$$= 2c_2|\Phi_{\mathbf{r}}| - 3c_3|\Phi_{\mathbf{r}}|^2 + 4u|\Phi_{\mathbf{r}}|^3$$

where in Gaussian unit $c_2 = m + \delta m$ with $m = \lambda - 12J_\pm, \delta m = \frac{9J_\pm e^2g^2J^c_\pm\Lambda}{\pi^2} + \mathcal{O}(e^2J^2_{z\pm})$, $c_3 = \frac{3J_\pm e^2g^2J^c_\pm}{\pi}\sqrt{6J_\pm e^2g^2}$, and $\Lambda \sim 1/a$ with a is microscopic lattice spacing. In physical unit, $\delta m = \frac{9J_\pm a^2e^2g^2\mu_0J^c_\pm\Lambda}{\pi^2\hbar^2} + \mathcal{O}(J^2_{z\pm}e^2)$, $c_3 = \frac{3J_\pm a^2e^2g^2\mu_0J^c_\pm}{\pi\hbar^2}\sqrt{\frac{6J_\pm a^2e^2g^2\mu_0}{\hbar^2}}$, $c_4 \equiv u = u_0 + \mathcal{O}(J^2_{z\pm}e^4)$.

The final free energy in real space takes the form,

$$F[\Phi^*_{\mathbf{r}}, \Phi_{\mathbf{r}}] = \int d^3r[c_2|\Phi_{\mathbf{r}}|^2 - c_3|\Phi_{\mathbf{r}}|^3 + c_4|\Phi_{\mathbf{r}}|^4] \tag{3.39}$$

with $c_2 = \lambda - 12J_\pm + \frac{16J_\pm a^2e_g^2g^2\mu_0J^c_\pm\Lambda}{\pi^2\hbar^2} + \mathcal{O}(e_g^2J^2_{z\pm})$, $c_3 = \frac{16J_\pm a^2e_g^2g^2\mu_0J^c_\pm}{3\pi\hbar^2}\sqrt{\frac{32J_\pm a^2e_g^2g^2\mu_0}{3\hbar^2}}$, $c_4 \equiv u = u_0 + \mathcal{O}(J^2_{z\pm}e_g^4)$ where we have used $e_g = \frac{3}{4}e$.

The location of QSL-AFM phase transition can be predicted directly from the free energy Eq. (3.39). We noticed previously that the coupling to gauge fields renormalizes the spinon gap (mass) m only by subleading correction $\delta m = \frac{16J_\pm a^2e_g^2g^2\mu_0J^c_\pm\Lambda}{\pi^2\hbar^2} +$

$\mathcal{O}(e_g^2 J_{z\pm}^2)$ (in physical unit). According to Eq. (3.39), it can be shown that the phase transition occurs at

$$c_2 = \frac{c_3^2}{4c_4} \tag{3.40}$$

Physically, the QSL to AFM phase transition is bosonic spinon condensation that occurs once the spinon becomes gapless. With c_3 and c_4 given as before, Eq. (3.40) suggests that the transition occurs at $m = \frac{c_3^2}{4c_4} - \delta m$. Since both terms on the right hand side are subleading to m, to lowest order approximation, the QSL-AFM phase transition therefore occurs at $m = \lambda - 12J_\pm = 0$ or equivalently $\lambda = 12J_\pm$. To compare this with gMFT result however, we have to carefully take into account an extra factor of $\frac{1}{4} = (\frac{1}{2})^2$ which arises from the fact that the gMFT ansatz [24] Eq. (3.17)

$$\langle s_\mu^- \rangle = \frac{1}{2}\cos\theta, \langle s_\mu^z \rangle = \frac{1}{2}\sin\theta\,\varepsilon_\mu \tag{3.41}$$

matches precisely with the spin-gauge field correspondence

$$s_{\mathbf{r},\mathbf{r}'}^z = E_{\mathbf{r},\mathbf{r}'}, s^\pm = e^{\pm iA_{\mathbf{r},\mathbf{r}'}} \tag{3.42}$$

only if we add factor half to the right hand side of the correspondence for $s^\pm$, i.e.,

$$s^\pm = \frac{1}{2}e^{\pm iA_{\mathbf{r},\mathbf{r}'}}$$

Therefore, since the $J_\pm$ term in the lattice gauge theory Eq. (3.12) consists of

products of bilinear term in bosonic spinon fields $\Phi^\dagger, \Phi$ and bilinear term in (exponential of gauge fields) s^+, s^-, it effectively predicts QSL-AFM phase transition at $\lambda = (\frac{1}{2})^2 12 J_\pm = 3J_\pm$.

We measure the size of first order phase transition in terms of the ratio of the shift in critical temperature between that of second order (without coupling to gauge field) and that of first order (due to coupling to gauge field) to the critical temperature of second order phase transition

$$\eta = \frac{J_\pm^{c\,\prime} - J_\pm^c}{J_\pm^c} \tag{3.43}$$

This can be computed from Eq. (3.39) and to lowest order approximation we obtain

$$\eta \sim \frac{a e_g^2 g^2 \mu_0 J_\pm^c}{\hbar^2} \ll 1 \tag{3.44}$$

This is a dimensionless quantity which indeed should be much smaller than unity because it is of order $\mathcal{O}(e_g^2)$. Using typical value of lattice spacing $a \sim 10$Å, spin exchange coupling $J_\pm \sim 0.1$ meV and standard value of parameters in QED as *trial* value where $e_g = 1.6 \times 10^{-19}$C and $g = 1$, we obtain $\eta \sim 10^{-8}$.

As a note, one may consider a definition of the size of first order phase transition in terms of the ratio between the jump of order parameter at the transition to the maximum value of order parameter deep in the ordered state. In our context, the ordered state is antiferromagnetic phase and the order parameter is the square root of bosonic spinon density $\langle \Phi \rangle$ that should be proportional to staggered magnetization

and is directly measurable in experiment. This is equally valid definition but involves deep ordered state in which Ginzburg-Landau-type free energy expansion ceases to be applicable. Definition based on the shift in critical energy scale, as is used in standard practice, involves only quantities near criticality where Ginzburg-Landau-type free energy expansion is fully applicable. Measurement of the shift in energy scale, which is the spin exchange coupling in this case, is far more challenging experimentally but is possible in principle [87].

The derivation of free energy discussed in this subsection assumes that the order parameter field Φ fluctuations do not affect the quantum phase transition and can be neglected. This is justified if the so-called Ginzburg criterion is satisfied, namely the energy scale interval within which the order parameter fluctuations are significant is sufficiently narrow so that these fluctuations can be neglected. To be precise [71]

$$\eta > t_{cr} = \frac{1}{32\pi^2}\frac{b^2}{a'}\frac{T_c^2}{\gamma^3} \tag{3.45}$$

where for our system $a' = 12J_{\pm}^c$,$b = 2u$,$T_c \equiv J_{\pm}^c$ and $\gamma = \frac{16}{3}J_{\pm}$.

So far, we have not specified explicitly the precise value of parameters in the field theory Eq. (3.11) such as the effective $U(1)$ gauge charge e (or e_g) and permeability ratio $g^2 = \frac{\mu}{\mu_0}$ whereas other parameters such as lattice spacing a and exchange coupling J's should be measurable and known for each specific compound. These parameters characterize the emergent electrodynamics and should be treated as phenomenological quantities determinable only from experiment and can in general have

rather different value than the standard value of parameters of QED in QFT. The effective speed of light in several pyrochlore quantum spin ice compounds is in the order of $v_p \sim J \ll c$ where c is the speed of sound [24]. This will imply rather large value of permeability ratio $g^2 = \frac{\mu}{\mu_0}$. In principle, v_p can be determined from specific heat measurement. It is basic result from statistical mechanics [85] that photons contribute term of the form

$$c_V^{ph} = \frac{4\pi^2 k_B^4 T^3}{15(\hbar v_p)^3} \tag{3.46}$$

to the specific heat at low temperatures, so that the speed of photon can be determined from the coefficient of the specific heat variation with temperature.

The gauge charge e_g on the other hand should be determinable from susceptibility measurement. This is because the photon-spinon coupling contributes to the photon-photon correlation function as well as spinon self energy and therefore enters the calculation of spinon-spinon two-point function $\chi^{\Phi}_{\mathbf{k},\omega} = \langle \Phi_{\mathbf{k},\omega} \Phi_{-\mathbf{k},-\omega} \rangle$ as well as the spin susceptibility $\chi^{\alpha\beta}_{\mathbf{k},\omega} \sim \langle S^{\alpha}_{\mathbf{k},\omega} S^{\beta}_{-\mathbf{k},-\omega} \rangle$. These two functions must therefore contain dependence on the gauge charge e_g. We do not pursue calculation of these quantities in this work. It is to be noted that gauge charge, just like electron charge, is nature's given fundamental quantity whose numerical value cannot be derived theoretically, but must be deduced empirically from experiment.

While the crucial Ginzburg criterion condition Eq. (3.45) involved in the theory presented here is expressed in terms of effective parameters measurable only by exper-

iments, at least for certain pyrochlore quantum spin ice compounds with appropriate chemical composition, the condition Eq. (3.45) should possibly be satisfied so that all results of this work are valid to those compounds.

3.5 Discussion

In this work, we consider pyrochlore spin ice in the quantum regime where short range exchange is the dominant interaction rather than dipolar interaction in classical regime. Quantum effects and geometric frustration work together to produce exotic phases in this quantum regime. Departing from the result of mean field study, we theoretically investigate quantum phase transition tuned by changing the spin exchange constants $J_{zz}, J_{\pm}, J_{z\pm}$. This is a challenging task experimentally since given a compound with a measured set of couplings, it corresponds to merely one point in the theoretical phase diagram. The quantum phase transition studied here is more feasible for experimental studies if we can find compound which microscopically is close to criticality. Pyrochlore compounds near quantum critical point have been the subject of intense research lately [86], aimed at discovering compounds with microscopic parameters that are located in the quantum critical regime. Applying pressure [87], magnetic field or chemical substitution (doping) to such compounds as indirect means to tune coupling constants is expected to drive the compound to cross the QSL-AFM phase boundary where the quantum criticality predicted in this work can be directly

verified.

We have treated bosonic spinon and gauge field explicitly and the interaction between them has been included in the free energy calculation. Other than these two excitations, there is also magnetic monopole which is gapped and plays important role especially at energies above the gap. Different from 2-d case where the magnetic monopoles of compact $U(1)$ gauge theory can lead to confinement and destroy the spin liquid state, in 3-d the monopoles are suppressed and so we have stable $U(1)$ QSL. This observation at the same time justifies our low energy effective theory derivation where the compactness of the gauge field is sacrificed. The presence of fractional excitations in pyrochlore quantum spin ice is itself an exciting question that has been investigated experimentally [88]. It is an open problem to include all these excitations and treat the interaction between them fully field theoretically. Another open problem of interest is to do similar study on the nature of quantum phase transition between $U(1)$ QSL and the so-called "Coulombic ferromagnet" (CFM) phase [24]. CFM is an interesting phase because it has ferromagnetic order but with spinon and photon as excitations rather than spin wave. We find that studying QSL-CFM phase transition using similar free energy description is a more formidable task and is therefore an open opportunity for further effort.

In conclusion, in this gauge theory picture, we obtain first order QSL-AFM quantum phase transition driven by gauge fluctuations treated at gauge theory level. We conclude that gauge fluctuations have driven the mean-field second order phase transi-

tion to first order one. We therefore obtain a fluctuation-induced first order quantum phase transition rather than the standard Ginzburg-Landau theory's continuous second order. To be more precise, this QSL-AFM phase transition is predicted to be weakly first order. The occurrence of this phenomenon reflects the $U(1)$ gauge theory structure of the Coulomb phases of pyrochlore quantum spin ice, which manifests an emergent quantum electrodynamics (QED).

Final point to note, this study begins with a general theoretical model represented by the Hamiltonian Eq. (3.1). One of the most actively studied pyrochlore compounds $Yb_2Ti_2O_7$ has spin exchange coupling constants which will place in ferromagnetic (FM) phase according to the theoretical phase diagram proposed in Ref. [24]. Once again, we need pyrochlore compounds whose spin exchanges will put them within $U(1)$ spin liquid phase near its boundary to AFM phase in order to test results predicted in this work.

Bibliography

[1] N. L. Schryer and L. R. Walker, J. Appl. Phys. 45, 5406 (1974).

[2] N. D. Mermin, Rev. Mod. Phys. 51, 591 (1979).

[3] T. H. R. Skyrme, Proc. R. Soc. London A 260, 127 (1961).

[4] C. Moutafis, S. Komineas, and J. A. C. Bland, Phys. Rev. B 79, 224429 (2009).

[5] P. W. Anderson, Mater. Res. Bull. 8, 153 (1973).

[6] P. A. Lee, Science 321, 1306 (2008).

[7] L. Balents, Nature 464, 199 (2010).

[8] H. T. Diep, Frustrated Spin Systems (World Scientific, Singapore, 2004).

[9] R. Moessner and S. L. Sondhi, Phys. Rev. B 63, 224401 (2001).

[10] S. Yan, D. A. Huse, and S. R. White, Science 332, 1173 (2011).

[11] J. A. Hertz, Phys. Rev. B 14, 1165 (1976).

[12] A. J. Millis, Phys. Rev. B 48, 7183 (1993).

[13] S. Sachdev, Quantum Phase Transitions (Cambridge University Press, Cambridge, 2011).

[14] C. Xu and S. Sachdev, Phys. Rev. B 79, 064405 (2009).

[15] J. S. Gardner, M. J. P. Gingras, and J. E. Greedan, Rev. Mod. Phys. 82, 53 (2010).

[16] J. Rossat-Mignod, in Proceedings of the Nato Advanced Study Institute on Systematics and the Properties of the Lanthanides, edited by S. P. Sinha (Reidel, Dordrecht, 1983), Chap. 7.

[17] B. C. den Hertog and M. J. P. Gingras, Phys. Rev. Lett. 84, 3430 (2000).

[18] S. V. Isakov, K. Gregor, R. Moessner, and S. L. Sondhi, Phys. Rev. Lett. 93, 167204 (2004).

[19] R. Moessner and J. T. Chalker, Phys. Rev. Lett. 80, 2929 (1998).

[20] C. L. Henley, Annu. Rev. Condens. Matter Phys. 1, 179 (2010).

[21] M. Hermele, M. P. A. Fisher, and L. Balents, Phys. Rev. B 69, 064404 (2004).

[22] K. A. Ross, L. Savary, B. D. Gaulin, and L. Balents, Phys. Rev. X 1, 021002 (2011).

[23] S. Onoda, J. Phys.: Conf. Ser. 320, 012065 (2011).

BIBLIOGRAPHY

[24] L. Savary and L. Balents, Phys. Rev. Lett. 108, 037202 (2012).

[25] I. Makhfudz, B. Kruger, and O. Tchernyshyov, Phys. Rev. Lett. 109, 217201 (2012).

[26] C. L. Chien, F. Q. Zhu, and J. G. Zhu, Phys. Today 60, 40 (2007).

[27] L. D. Landau and E. M. Lifshitz, Phys. Z. Sowjetunion 8, 153 (1935).

[28] T. L. Gilbert, IEEE Trans. Magn. 40, 3443 (2004).

[29] A. A. Thiele, Phys. Rev. Lett. 30, 230 (1973).

[30] K.Y. Guslienko, B. A. Ivanov, V. Novosad, Y. Otani, H. Shima, and K. Fukamichi, J. Appl. Phys. 91, 8037 (2002).

[31] S.-B. Choe, Y. Acremann, A. Scholl, A. Bauer, A. Doran, J. Stohr, and H. A. Padmore, Science 304, 420 (2004).

[32] J. P. Park and P. A. Crowell, Phys. Rev. Lett. 95, 167201 (2005).

[33] K.Y. Guslienko, X. F. Han, D. J. Keavney, R. Divan, and S. D. Bader, Phys. Rev. Lett. 96, 067205 (2006).

[34] B. Kruger, A. Drews, M. Bolte, U. Merkt, D. Pfannkuche, and G. Meier, Phys. Rev. B 76, 224426 (2007).

[35] A. P. Malozemoff and J. C. Slonczewski, Magnetic Domain Walls in Bubble Materials (Academic, New York, 1979).

[36] M. Hehn, K. Ounadjela, J.-P. Bucher, F. Rousseaux, D. Decanini, B. Bartenlian, and C. Chappert, Science 272, 1782 (1996).

[37] T. Fukumura, H. Sugawara1, T. Hasegawa, K. Tanaka, H. Sakaki, T. Kimura, and Y. Tokura, Science 284, 1969 (1999).

[38] S. Komineas, C. A. F. Vaz, J. A. C. Bland, and N. Papanicolaou, Phys. Rev. B 71, 060405 (2005).

[39] G. D. Skidmore, A. Kunz, C. E. Campbell, and E. D. Dahlberg, Phys. Rev. B 70, 012410 (2004).

[40] U. K. Rößler, A.N. Bogdanov, and C. Pfleiderer, Nature (London) 442, 797 (2006).

[41] S. Mühlbauer, B. Binz, F. Jonietz, C. Pfleiderer, A. Rosch, A. Neubauer, R. Georgii, and P. Boni, Science 323, 915 (2009).

[42] X. Z. Yu, Y. Onose, N. Kanazawa, J. H. Park, J. H. Han, Y. Matsui, N. Nagaosa, and Y. Tokura, Nature (London) 465, 901 (2010).

[43] S. X. Huang and C. L. Chien, Phys. Rev. Lett. 108, 267201 (2012).

[44] X. Yu, M. Mostovoy, Y. Tokunaga, W. Zhang, K. Kimoto, Y. Matsui, Y. Kaneko, N. Nagaosa, and Y. Tokura, Proc. Natl. Acad. Sci. U.S.A. 109, 8856 (2012).

BIBLIOGRAPHY

[45] J. Zang, M. Mostovoy, J. H. Han, and N. Nagaosa, Phys. Rev. Lett. 107, 136804 (2011).

[46] O. A. Tretiakov, D. Clarke, G.-W. Chern, Y. B. Bazaliy, and O. Tchernyshyov, Phys. Rev. Lett. 100, 127204 (2008).

[47] D. J. Clarke, O. A. Tretiakov, G.-W. Chern, Y. B. Bazaliy, and O. Tchernyshyov, Phys. Rev. B 78, 134412 (2008).

[48] W. Doring, Z. Naturforsch. 3A, 373 (1948).

[49] G. Tatara, H. Kohno, and J. Shibata, Phys. Rep. 468, 213 (2008).

[50] S. A. Langer, R. E. Goldstein, and D. P. Jackson, Phys. Rev. A 46, 4894 (1992).

[51] A. B. Kashuba and V. L. Pokrovsky, Phys. Rev. B 48, 10335 (1993).

[52] M. Seul and D. Andelman, Science 267, 476 (1995).

[53] M. J. Donahue and D. G. Porter, NIST Report No. NISTIR 6376, 1999, http://math.nist.gov/oommf.

[54] O. Petrova and O. Tchernyshyov, Phys. Rev. B 84, 214433 (2011).

[55] M. Mochizuki, Phys. Rev. Lett. 108, 017601 (2012).

[56] Y. Onose, Y. Okamura, S. Seki, S. Ishiwata, and Y. Tokura, Phys. Rev. Lett. 109, 037603 (2012).

BIBLIOGRAPHY

[57] I. Makhfudz, arXiv:1307.5804 (2013)(Accepted for publication in Phys. Rev. B).

[58] P. W. Anderson, Science 235, 1196 (1987).

[59] http://web.physics.ucsb.edu/ balents/projects/pyrochlores.html

[60] S. Onoda and Y. Tanaka, Phys. Rev. Lett. 105, 047201 (2010).

[61] S. Onoda and Y. Tanaka, Phys. Rev. B 83, 094411 (2011).

[62] L. -J. Chang, S. Onoda, Y. Su, Y.-J. Kao, K.-D. Tsuei, Y. Yasui, K. Kakurai, and M. R. Lees, Nature Commun. 3, 992 (2012).

[63] H. R. Molavian, M. J. P. Gingras, and B. Canals, Phys. Rev. Lett. 98, 157204 (2007).

[64] S. H. Curnoe, Phys. Rev. B 78, 094418 (2008).

[65] T. Senthil, L. Balents, S. Sachdev, A. Vishwanath, and M. P. A. Fisher, Phys. Rev. B 70, 144407 (2004).

[66] M. Kardar, Statistical Physics of Fields (Cambridge University Press, Cambridge, 2007).

[67] J. Cardy, Scaling and Renormalization in Statistical Physics (Cambridge University Press, Cambridge, 1996).

[68] V. L. Berezinskii, Sov. Phys. JETP 34, 610 (1972).

BIBLIOGRAPHY

[69] J. M. Kosterlitz and D. J. Thouless, Journal of Physics C: Solid State Physics 6, 1181 (1973).

[70] T. Senthil, A. Vishwanath, L. Balents, S. Sachdev, and M. P. A. Fisher, Science 303, 1490 (2004).

[71] B. I. Halperin, T. Lubensky and S. K. Ma, Phys. Rev. Lett. 32, 292 (1974).

[72] S. Coleman and E. Weinberg, Phys. Rev. D 7, 1888 (1973).

[73] D. Belitz, T. R. Kirkpatrick, and T. Vojta, Phys. Rev. Lett. 82, 4707 (1999).

[74] A. V. Chubukov, A. M. Finkelstein, R. Haslinger, and D. K. Morr, Phys. Rev. Lett. 90, 077002 (2003).

[75] A. S Ferreira and M. A Continentino, J. Stat. Mech. (2005) P05005.

[76] D. Belitz and T. R. Kirkpatrick, Phys. Rev. Lett. 89, 247202 (2002).

[77] J.-H. She, J. Zaanen, A. R. Bishop, and A. V. Balatsky, Phys. Rev. B 82, 165128 (2010).

[78] G. Misguich, D. Serban, and V. Pasquier, Phys. Rev. Lett. 89, 137202 (2002).

[79] S.B. Lee, S. Onoda, and L. Balents, Phys. Rev. B 86, 104412 (2012).

[80] The details and derivation are given in the subsection following this section.

[81] J. W. Orland and H. Negele, Quantum Many-Particle Systems (Westview Press, USA, 1998).

BIBLIOGRAPHY

[82] M. Peskin and D. Schroeder, Introduction to Quantum Field Theory (Perseus Books, Massachusetts, 1995).

[83] M. Srednicki, Quantum Field Theory (Cambridge University Press, Cambridge, 2007).

[84] I. F. Herbut, A Modern Approach to Critical Phenomena (Cambridge University Press, Cambridge, 2007).

[85] K. Huang, Statistical Mechanics (John Wiley and Sons, New York, 1987).

[86] Z. L. Dun, E. S. Choi, H. D. Zhou, A. M. Hallas, H. J. Silverstein, Y. Qiu, J. R. D. Copley, J. S. Gardner, and C. R. Wiebe, Phys. Rev. B 87, 134408 (2013).

[87] I. A. Zaliznyak, D. C. Dender, C. Broholm, and D. H. Reich, Phys. Rev. B 57, 5200 (1998).

[88] T-H. Han, J. S. Helton, S. Chu, D. G. Nocera, J. A. Rodriguez-Rivera, C. Broholm and Y. S. Lee, Nature 492, 406 (2012).

Vita

Imam Makhfudz obtained his undergraduate degree in electrical and electronic engineering from Nanyang Technological University, Singapore in 2005 (B. Eng. with First Class Honours). He obtained Master's (M.Sc.) degree in physics from National University of Singapore in 2008. He then enrolled in PhD program in physics at Johns Hopkins University in 2008. Upon defending his PhD Dissertation, Imam Makhfudz will begin post-doctoral work at Laboratoire de Physique Théorique in Toulouse, France in January 2014.